Rialtas na hÉireann
Government of Ireland

Geological Survey
Suirbhéireacht Gheolaíochta
Ireland | Éireann

Tellus Waterford Test Line:

Evaluation of coincident ERT and airborne EM resistivity profiles

Document Information

Project title: Tellus Waterford Test Line: Evaluation of coincident ERT and airborne EM resistivity profiles Current Document version: V3

Prepared By	Date	Comment
S. Lilburn	14/02/2022	V3

Reviewed by	Date	Comment
M. Muller	10/01/2022 – 15/02/2022	
J. Hodgson	10/01/2022 – 15/02/2022	

Approved By	Date	Comment
J. Hodgson	17/02/2022	Geological Survey Ireland

Version History

Ver. No.	Ver. Date	Comment	By
V3	16/02/2022	First published version of report	S. Lilburn

Table of Contents

Executive summary

A ground Electrical Resistivity Tomography (ERT) survey was undertaken in October 2021 along the 4.4 km on-land portion of the Waterford Test Line with the intention of collecting comparative ground data for the Tellus airborne electromagnetic (EM) survey. The test line is located approximately 19 km southwest of Waterford City, near the villages of Bunmahon and Kill, and is flown repeatedly during the Tellus airborne geophysical survey for instrument calibration, data QC and data merging purposes. The primary aim of this survey was to investigate how the resistivity structure of the subsurface along the test line is imaged by ERT and how the ground data compare to Tellus airborne EM inversion data. This was done by comparing the ranges of resistivity values, the presence and dimensions of resistive and conductive bodies in the subsurface, and the depths at which boundaries between bedrock and overburden, and other subsurface layers, are resolved in the respective (ground and airborne) inverse modelled resistivity sections. The investigation also included a comparison of inversion models produced from ERT data collected using three distinct electrode array configurations (Schlumberger, Wenner Alpha and Dipole-Dipole) and examined the repeatability of the ERT data by comparing data acquired along a 395 m stretch of the Waterford Test Line during a previous (2018) Tellus ground ERT survey with data measured along coincident profiles in this 2021 survey.

ERT data were recorded over ten individual profiles along the test line using the *ARES II* 10-channel automatic resistivity and IP system by GF Instruments and inverted using *Res2Dinv* software. Airborne EM inversion model sections, using data from 20 repeat test line flights, were derived by 1-D inversion of the eight data components (in-phase and quadrature components at four frequencies) at each measurement location on each line using *aempy* modelling software, and subsequent gridding of the individual 1-D resistivity-depth models to give 2-D cross-sections. ERT and EM inversion model resistivity data were gridded using *Geosoft Oasis Montaj* software and compared both visually and statistically.

Good agreement was observed between the models corresponding to the different ERT array types (except for some profiles along which the dipole-dipole array gave dissimilar results). The Schlumberger and Wenner RMS errors were very similar with typically low errors, giving confidence in these models.

Resistivity values were largely found to be comparable for ERT and airborne EM resistivity models, with ratios of (mean EM resistivity):(mean ERT resistivity) falling between 0.7 and 1.25 except where ERT model RMS errors were high (⩾ 10 %). Where ERT and EM models were visually similar and imaged the same subsurface units, the depths and resistivity values at which the unit boundaries were defined were broadly in agreement between the models. A 'smoothed out' appearance of some features in EM models was noted, however, and attributed to the lower lateral and vertical resolution of the EM data compared to the ERT data.

The ERT and EM models were notably different along several profiles, and furthermore, in some cases the two EM lines considered for closer examination were themselves dissimilar. A comparison of the 2018 and 2021 ERT (Wenner array) models also revealed some variability between successive ground ERT surveys. An investigation into the repeatability of the airborne EM data, and perhaps also the ground ERT data, is therefore recommended to better assess the observed variability.

1. Introduction

1.1. Background to the Tellus Geophysical Survey

Tellus is a national programme, managed by Geological Survey Ireland (GSI) and funded by the Department of the Environment, Climate and Communications (DECC), aimed at collecting geophysical and geochemical data across the island of Ireland to support environmental and natural resource management. The geophysical survey commenced in the Republic of Ireland in 2011 with the Tellus Border project (funded by the INTERREG IVA programme of the European Regional Development Fund) and follows on from the Tellus surveys of Northern Ireland which ran from 2004 to 2007. Eleven distinct survey blocks have been flown in the Republic of Ireland to date and all data are freely available at www.gsi.ie/Tellus.

The Tellus airborne geophysical survey collects magnetic, electromagnetic (EM) and radiometric (gamma-ray spectrometry) from a low-flying, all metal, fixed-wing, de Havilland DHC-6 Twin Otter airplane operated by Sander Geophysics Ltd. The aircraft is fitted with a magnetometer, frequency-domain EM system and gamma-ray spectrometer as well as altimeter systems, a barometric pressure sensor, an outside air temperature probe, DGPS and digital video imaging systems. Further details of the survey equipment may be found in Ture (2020) and SGL (2019). Table 1 below details the flight pattern.

Table 1: Flight pattern for airborne geophysical survey.

Traverse line spacing	200 m
Tie line spacing	2000 m
Traverse line heading	165 / 345°
Tie line heading	75 / 255°
Nominal flying height (rural / urban)	60 m / 240 m
Nominal flying speed	60 m/s
Projection/Datum	Irish Transverse Mercator (ITM)

1.2. Test Line

1.2.1. Purpose of Test Line

A repeat test line was established for airborne data QC purposes as part of ongoing calibration testing, to assess noise and the repeatability of measurements, and to facilitate the merging of datasets collected during different years and seasonal conditions. The test line is flown at the beginning and near the end of each survey at four flight elevations (60, 90, 120 and 150 m above ground level) in both directions. In addition to allowing direct comparisons to be made between surveys, repeat flights over the test line allow the sensitivity of the measurements to variations in altitude and rainfall, as well as any environmental impacts, to be investigated.

1.2.2. Bundoran and Waterford Test Lines

An initial test line was developed near the town of Bundoran in County Donegal, which extended from 577167.238 m E, 859053.683 m N to 578695.063 m E, 853336.292 m N (ITM) and crossed from sea (Donegal Bay) to onshore. The line is 6 km long and traverses variable bedrock and superficial geology as well as coastal transition zone and seawater. The new Waterford test line was established to avoid logistical difficulties associated with the Bundoran test line as the airborne survey progressed southwards and has been flown since 2019 (block A7 onwards). The Waterford test line is described in further detail in section 3.

FEM calibration requires flying over seawater. Initially, an area over Donegal Bay was chosen where the water depth reached > 60 m and conductivity and temperature measurements had been taken at one metre intervals from surface to seafloor by the Marine Institute, allowing an estimation of the conductivity variation with depth to be made. The offshore portion of the new Waterford test line has a sea surface salinity within 0.1 g/L of that measured over Donegal Bay in 2017 (according to the Irish Marine Atlas), thus similar resistivity and thermal characteristics are expected. This portion of the Waterford test line replaces Donegal Bay for EM over-seawater calibration.

1.3. Ground Survey Rationale and Objectives

The aim of the ground Electrical Resistivity Tomography (ERT) survey was to collect comparative ground data for the Tellus airborne EM survey. These data are intended to facilitate a comparison of how the resistivity structure of the subsurface along the Waterford test line is imaged by the respective (airborne and ground) methods in terms of:

(a) the range of resistivity values modelled over a given section of the line,
(b) the shape, size and orientation of subsurface features modelled using the airborne EM data and ERT data for three different array configurations, and
(c) the depths at which bedrock and other subsurface strata are delineated.

2. Geophysical Surveying Methods

2.1. Airborne Electromagnetic (AEM)

2.1.1. General

A broad range of electromagnetic surveying techniques and instrumental systems exist today with a wide variety of applications including mineral and hydrocarbon exploration, geological, sea ice thickness and permafrost mapping, and environmental and archaeological investigations (Reynolds 2011). EM techniques involve the generation of a primary electromagnetic field by a transmitter coil which travels through air and subsurface media and is modified in the latter. When primary EM waves interact with a conductive body in the subsurface they induce eddy (alternating) currents within the conductor which in turn generate their own secondary EM field. A receiver coil detects both this secondary field and the primary field which has travelled through the air, and the measured response is the resultant of both fields, which “differs in both phase and amplitude relative to the unmodulated primary field” (Reynolds 2011). This EM response provides information about the electrical properties of subsurface materials which may relate to a number of factors such as geochemistry, mineralogy, porosity and permeability, pore-fluid salinity as well as temperature and pressure (Ture and Muller 2020).

Electromagnetic methods are classified as either time-domain (TEM), whereby measurements are made as a function of time, or frequency-domain (FEM) which involves taking measurements at a number of different frequencies. The lower frequencies perform well in mapping relatively deep conductive bodies such as base metal ore deposits, imaging to depths of 40 – 100 m depending on the resistivities of the subsurface materials, while the higher frequencies are sensitive at shallower depths and more resistive bodies for use in environmental and engineering applications.

2.1.2. Tellus AEM Survey

The Tellus survey utilises the FEM method (with the exception of the North Midlands block, in which TEM data were collected) to collect electromagnetic data at four frequencies (912, 3005, 11962, 24510 Hz) (Ture and Hodgson 2017), providing high vertical resolution and improved depth discrimination capability compared to two-frequency systems (Beamish *et al.* 2006), and facilitating both 1-D and 2-D inversion modelling. The survey aircraft has wing-tip mounted coils with a transmitter-receiver separation of 21.4 m. Data are collected at a sample rate of 40 Hz and later decimated to 10 Hz during processing by the contractor. System calibrations include EM system orthogonality and over-seawater calibration. EM data are particularly susceptible to cultural interference (e.g. power lines, electric fences) which can create noise that is difficult to remove, thus 50/60 Hz power line monitor data are recorded during flight and can be used to identify potential interference from such sources. The quality of the data is also affected by high-fly zones, with EM data collected at a survey height >150 m considered to be less reliable and of limited use.

Orthogonal in-phase and quadrature components of the EM response at each frequency are recorded and subsequently processed independently of one another, providing eight data components at each measurement location (Muller and Hodgson 2020). Single-frequency resistivity products (maps and flight line data) are derived using approximate, half-space resistivity transformations to model each frequency separately and independently. From 2019 (A5 block) onwards, Tellus geophysical products have also included EM inversion resistivity models produced by formal 1-D inversion of all eight EM data components simultaneously at each measurement site (detailed in section 4.2.2), providing better depth constraints and allowing users to produce more reliable vertical geological cross-sections (Muller and Hodgson 2020).

2.2. Electrical Resistivity Tomography (ERT)

Electrical Resistivity Tomography, also known as Electrical Resistivity Imaging (ERI) measures the resistivity (or conductivity) of the subsurface using the principle of Ohm's Law, which can be expressed as:

$$V = I.\rho.\frac{l}{A}$$

Where V is the voltage measured between two electrodes, I is the current applied, l and A are the path length and cross-sectional area along/through which the current flows, respectively, and ρ is the resistivity of the material through which the current passes. Most ERT surveys, and indeed all of the profiles presented in this report, employ an array of four electrodes for each measurement consisting of two current electrodes (C_1 and C_2), which inject a current into the ground, and two potential electrodes (P_1 and P_2) which measure the corresponding potential difference. The relative positions of, and spacing between, these electrodes are determined by the choice of array configuration (discussed in section 2.4 below). This electrode geometry is described in the geometric factor (K) required to calculate the resistivity of the material from the applied current and resulting voltage. Since the subsurface is an inhomogeneous medium, the value for resistivity obtained for each set of four electrodes (C_1, C_2, P_1, P_2) is an *apparent* resistivity, rather than the true resistivity, and is not a physical property of the subsurface media (Reynolds 2011).

In ERT, electrodes are laid out with a constant separation along the profile to be surveyed and apparent resistivities are measured for successive sets of current and potential electrodes, shifting laterally along the profile by one electrode separation for each iteration and repeating this process with increasing separation (i.e., obtaining a value between electrodes [1,2,3,4], [2,3,4,5],…., then [1,3,5,7], [2,4,6,8],...., [1,4,7,10], etc.) to measure apparent resistivities along the profile at a number of (depth) levels (the greater the electrode separations, the greater the depth of imaging). These values are plotted and interpolated in two dimensions to generate an apparent resistivity pseudo-section from which true resistivities can be modelled and interpreted.

2.3. Induced Polarization (IP)

Induced polarization surveys are carried out using conventional electrical resistivity electrode configurations and effectively measure the *polarizability* of subsurface media. Current is conducted in the subsurface by the movement of ions in pore fluid (e.g. groundwater) travelling through interconnected pores and fractures. Grains of conductive materials (e.g. metal sulphide) interrupting these pathways build up charge and become polarized, creating a potential difference ('over-potential') across the grain which decays in a finite time when the current is switched off and ions diffuse back through the pore fluid. IP surveys are particularly useful in finding disseminated metallic ores because the charge build up occurs at the surface these grains, thus the IP response is greater where the surface area of such materials is large (Reynolds 2011). Polarization can also occur where negative charge builds up in the electrolyte (pore fluid) itself when constrictions or clay particles are present in fluid channels, preventing normal ionic diffusion and establishing a potential (Reynolds 2011).

The IP survey discussed in this report utilised the time-domain method. This involves switching the current on and off in 'pulses,' with an initial voltage measurement made at a fixed time after the current is switched off and subsequent measurements of the over-potential decay made over very short time periods at fixed intervals. The observed voltage is the sum of the voltage due the applied current and the over-potential (polarization voltage). Dividing the integral of the over-potential decay by the observed voltage gives a parameter referred to as the *apparent chargeability* which is diagnostic of the geological medium for given survey parameters (e.g., charging time) (Reynolds 2011).

2.4. Electrode Array Configurations for Ground Surveys

The apparent resistivity measured depends on the geometry of the electrode array. Each configuration is sensitive to different subsurface structures and has various advantages and disadvantages relating to section coverage (depth range and side coverage), measurement resolution and time, availability of data acquisition, processing and inversion software, and measurement conditions such as susceptibility to electrical noise and required transmitter power output (Reynolds 2011, GF Instruments, s.r.o. 2019). This section discusses the three array configurations used in this ground resistivity survey.

2.4.1. Schlumberger

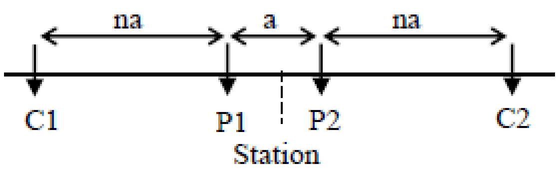

Figure 1: Schlumberger array [source: ARES II User Manual v1.5].

In the Schlumberger, or 'Wenner-Schlumberger,' array the current electrodes are positioned outside the potential electrodes and the separation *na* (in figure 1) is greater than or equal to five times the potential electrode separation, *a* (Reynolds 2011). This array can be used effectively for a number of applications, particularly for imaging horizontal or near-horizontal layers, providing moderate vertical resolution, depth of penetration (approx. 1/5 of the maximum C_1-C_2 distance used), and sensitivity to lateral inhomogeneities (GF Instruments, s.r.o. 2019).

2.4.2. Wenner Alpha

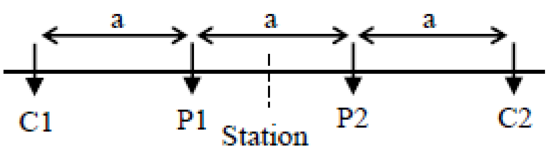

Figure 2: Wenner Alpha array [source: ARES II User Manual v1.5].

The Wenner-alpha array has similar imaging applications to the Schlumberger array, and is a suitable alternative where the latter is affected by electrical noise. It exhibits the fastest measurement times and has a greater vertical resolution, making it particularly useful where horizontally-layered media are concerned, however, its depth penetration is poorer (approx. 1/6 of maximum C_1-C_2 distance) thus it is unsuitable for investigating deeper structures (Reynolds 2011, GF Instruments, s.r.o. 2019). The Wenner Alpha is the most commonly used Wenner array configuration and features a constant separation, *a*, between all four electrodes.

2.4.3. Dipole-Dipole

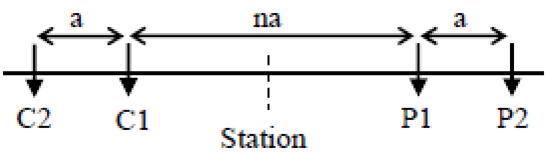

Figure 3: Dipole-Dipole array [source: ARES II User Manual v1.5].

The dipole-dipole array is especially suited to detecting vertical subsurface structures and deeper features, while its sensitivity to "deep lateral resistivity variations [make it] an unsuitable array for depth sounding" and give poor vertical resolution (Reynolds 2011). The dipole-dipole array features two pairs of closely spaced current and potential electrodes (as in figure 3), with a greater separation between the pairs (*na* > *a*). It offers greater depth penetration and side coverage than the Wenner Alpha array but with longer measurement times. A notable limitation of this array is its susceptibility to artificial electrical noise (GF Instruments, s.r.o. 2019).

3. Study Area

3.1. Waterford Test Line

The Waterford test line is located approximately 19 km southwest of Waterford city in the southeast of Ireland (figure 4). The northern end of the line lies 0.65 m west of the village of Kill and the southern end (of the on-land portion) lies roughly 2.76 km east of Bunmahon (see figure 5). Details of the line are given in table 2.

Figure 4: Location of the study area, approximately 19 km southwest of Waterford city in the southeast of Ireland. The red rectangle corresponds to the full extent of the map shown in figure 5.

Table 2: Properties of the Waterford test line.

Total length	6 km
Length of on-land portion (excluding coastal transition zone), shown in figure 2	4.4 km
Start (on-land, SE)	Easting: 646017.5577, Northing: 598633.8962 (ITM)
Finish (on-land, NW)	Easting: 644878.2414, Northing: 602883.5465 (ITM)
Heading	165 / 345°

Figure 5: On-land portion of Waterford test line.

3.2. Site Background

3.2.1. Bedrock Geology

According to the Geological Survey Ireland (GSI) 1:100,000 Bedrock Geology map (figure 6) the test line traverses two distinct lithological units. The southernmost 1850 m (approx.) of the line is underlain by laminated shale and siltstone and peperite of the Dunabrattin Formation, while the Campile Formation underlying the northern portion of the line comprises rhyolitic volcanics and grey and brown slates. The line also intersects discrete shale units within this formation. With the exception of exposed rock/cliff faces along the coastline, bedrock outcrops are relatively scarce in the vicinity of the test line so the locations of lithological boundaries may not be exactly as mapped in places.

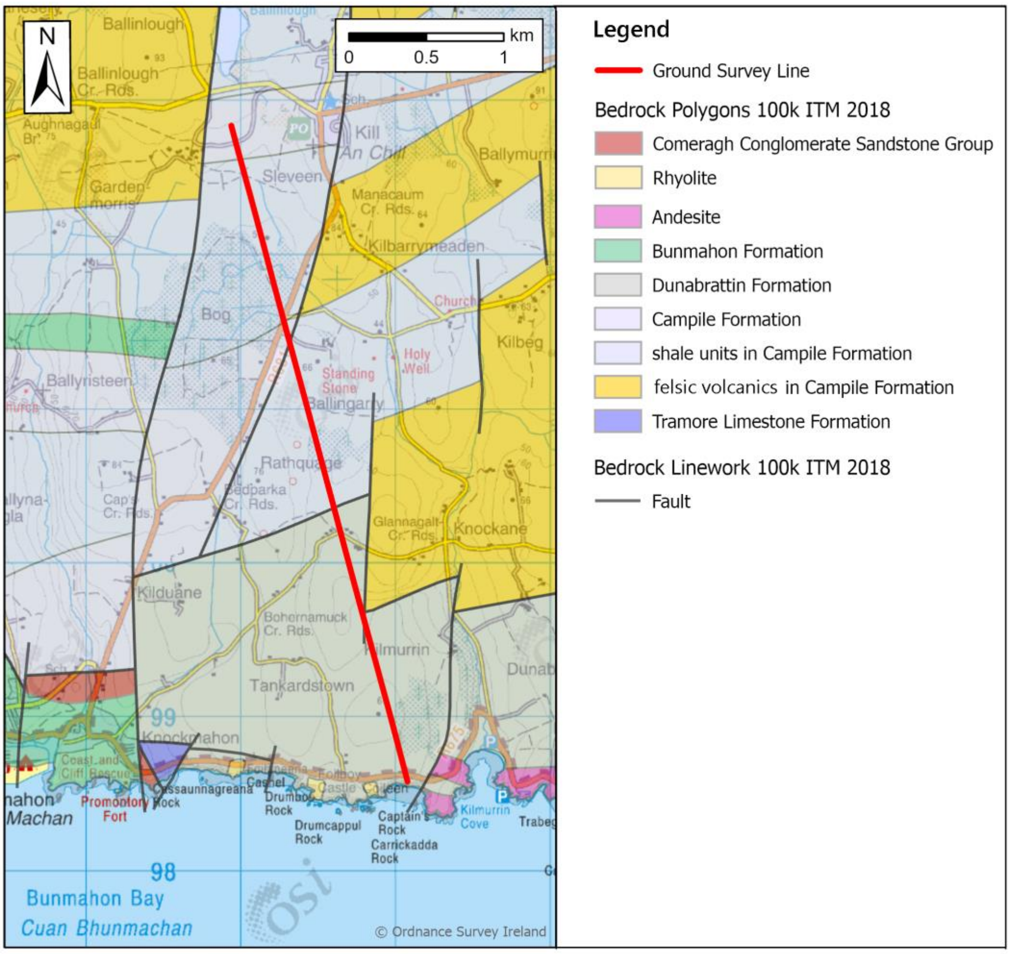

Figure 6: Bedrock Geology (GSI, 1:100,000) of the study area.

3.2.2. Quaternary Geology

The subsoil geology in the area (figure 7) is dominated by tills derived from acidic volcanic rocks, with localised deposits of alluvium. One such alluvium deposit intersects the test line approximately 1260 m from its southern end.

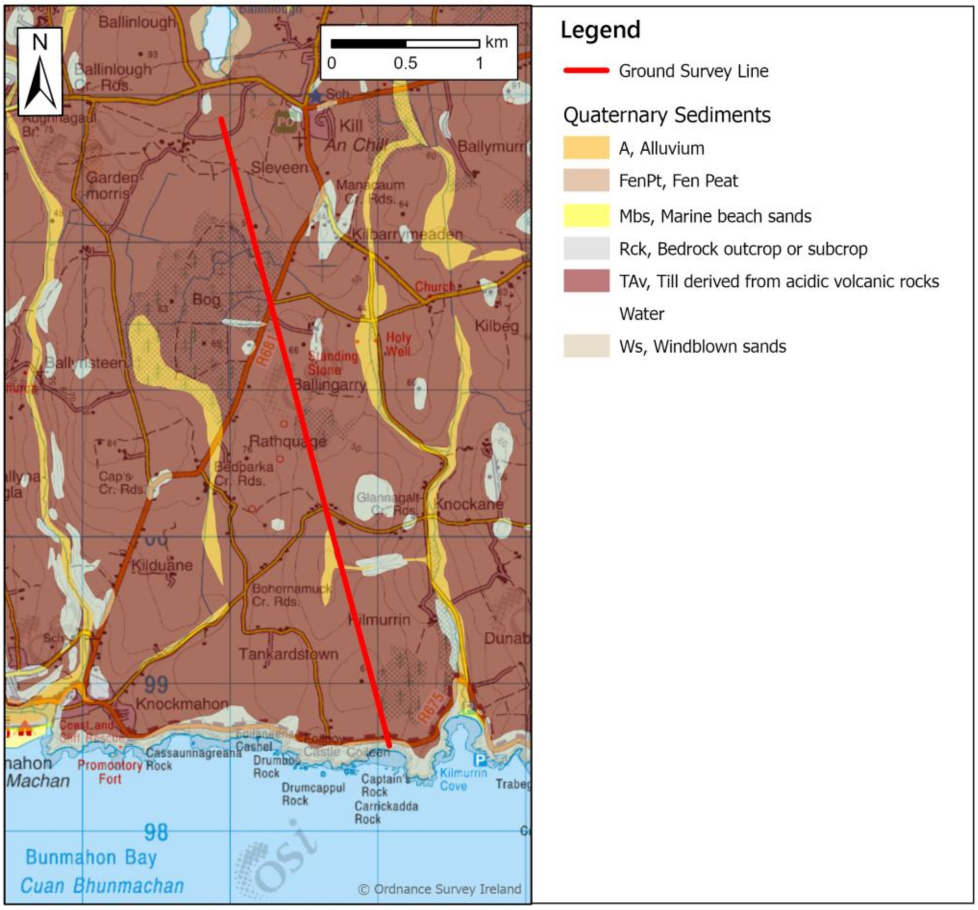

Figure 7: Quaternary Geology (GSI, 1:50,000) of the study area.

3.2.3. Land Use

The Ordnance Survey Ireland (OSI) 1:50,000 Discovery Series basemap (figure 5) shows an area of bog and coniferous woodland towards the northern end of the line as well as two smaller areas of coniferous woodland in the centre and at the southern end of the line, although the latter was not encountered on the ground. The line crosses major (regional) roads at approximately 30 m and 3100 m (from its southern end) and minor roads/laneways at 1650 m, 2990 m and 4280 m.

The land in the vicinity of the line is primarily pasture, with an isolated area of coniferous forest and transitional woodland shrub, according to the CORINE Land Cover database (Copernicus 2018).

3.2.4. Previous Investigation

A previous geophysical ground investigation on the Waterford test line was carried out in September 2018 and is detailed in Crowley and Ture (2018). The investigation consisted of an ERT survey (GF Instruments *ARES II* system, 395 m long profile, 5 m electrodes spacing, Wenner Alpha array) coinciding approximately with profiles 'Bun2' and 'Bun10' of this survey (October 2021), a radiometric survey between 646019 E, 598634 N and 645312 E, 601273 N (ITM) (Scintrex GIS-5 portable gamma-ray spectrometer, 20 m measurement interval), and a magnetic survey (Scintrex ENVI-MAG portable magnetometer, 20 m measurement interval). The test line had not yet been flown at the time of this investigation so ground test data were compared to data collected along an adjacent production line (L1098, Tellus Waterford airborne survey (2016)), running parallel to, and located 100 m from, the test line. An EM resistivity cross-section model of a portion of this production line, with a length matching the extent of the ERT profile, was generated by 1-D inversion using EMIGMA software.

Similarities were observed between the airborne EM resistivity model and the ground ERT inversion model, with an area of shallower bedrock discernible in the northernmost part of each model section. Crowley and Ture (2018) also observed similar trends between airborne and ground radiometric data while noting significant differences in the spectrometer crystal volume and footprint between the two surveys. Correlation was also observed between the ground and airborne magnetic data, with patterns observed that could be rationalized in terms of the underlying geology.

4. Methodology

4.1. Electrical Resistivity Tomography (ERT) and Induced Polarization (IP) Surveys

4.1.1. Logistics

The ground survey was carried out between the 4th and 8th of October 2021. A field base was established in Dungarvan, Co. Waterford for the week, from which the field team travelled to the survey site(s) each day.

4.1.2. Equipment

Ground geophysical data were collected using the *ARES II* 10-channel automatic resistivity and IP system by GF Instruments. In this particular survey, 2D multi-electrode measurements were made using a single channel to obtain apparent resistivity and induced polarization sections. Survey equipment consisted of the ARES II unit, seven multi-electrode cables with junction boxes, a T-piece (for connection of multi-electrode cable sections), stainless steel electrodes, O-rings (elastics) for connecting cable outlets to electrodes, DC power source (12 V lead-acid car battery) and connection cable, USB cable (for data export), mallet hammer, tape measure and ranging rods.

4.1.3. Data Collection

- A handheld GPS was used to locate pre-defined waypoints along the test line for each profile, and ranging rods were used to mark the beginning and end of each profile, with a third rod established near the mid-point of the line (visible from both ends) to ensure the electrodes and cable sections were laid out in a straight line.
- Using a tape measure, a straight line of stainless steel electrodes, spaced 5 m apart, was installed along the full length of the profile. The electrodes were hammered into the ground as deep as was practicable to mimimise the electrical contact resistance between the ground and each electrode. Saline solution was added to the soil around any electrode where the equipment indicated a high resistance (e.g., on a gravel road where the electrode could not penetrate the ground to sufficient depth).
- Elastic bands (O-rings) were used to attach the electrodes to the multi-cable outputs.

- Cable sections were connected using junction boxes (one junction box attached to the end of the final cable section; no junction box at the beginning of the first cable section).
- The T-piece was used to connect the *ARES II* unit between any two cable sections (i.e., not at either end of the profile) where desired.
- The unit was connected to the 12 V DC power supply (car battery).
- Upon starting the measurement, the equipment identified accessories and informed the user of the number of connected electrodes and the number required for the measurement. These were checked to ensure the information was correct before continuing each measurement. Dummy electrodes were then specified, where applicable.
- The equipment then tested the contact resistances at each electrode. Where all resistances were sufficiently low the measurement was continued. Where resistances were high the electrode array was checked to ensure all apparatus was set-up and functioning correctly. Saline solution was added to the soil surrounding the electrodes where necessary.
- Data were saved to a portable USB flash drive upon completion of each measured profile.

The co-ordinates of the 'start' and 'end' points of each resistivity profile measured along the test line in October 2021 are given in table 3. These co-ordinates correspond to the lines shown in figure 8. 'Global Distance on Line' is measured relative to the start of the on-land portion of the test line, denoted by "START" in figure 8. Figure 9 shows how the topography and bedrock geology (from GSI's 1:100K Bedrock Geology map) vary between profiles along the line.

Table 3: Positions of measured profiles on the test line, co-ordinates of the beginning and end of each profile, the total profile length, and the number of electrodes used. Note: "S" denotes the southern end (beginning) of each profile and "N" denotes the northern end. Distances prefixed with "N" in the *Global Distance on Line* column indicate that the ERT profile was laterally offset from the desired line due to obstacles on the ground. Bun7x is a single Schlumberger recording made on profile Bun7, but with an addition cable (8 electrodes) installed to the north. The Bun7x model is not presented in the report.

ERT Profile	*Global Distance on Line (m)*	*Easting (ITM)*	*Northing (ITM)*	*Profile Length {m)*	*No. of Electrodes*
Bun1 S	1520	645623.5	600101.8	150	31
Bun1 N	1670	645584.9	600246.7		
Bun2 S	1690	645579.8	600266.1	220	45
Bun2 N	1910	645523.1	600478.7		

Bun3 S	N200	645968.1	598826.3	225	46
Bun3 N	N425	645926.4	599045.1		
Bun4 S	550	645877.5	599165.8	275	56
Bun4 N	825	645805.4	599431.1		
Bun5 S	N2440	645376.8	600987.0	275	56
Bun5 N	N2715	645305.2	601251.2		
Bun6 S	705	645836.9	599315.3	275	56
Bun6 N	980	645764.4	599580.6		
Bun7 S	3580	645091.6	602091.9	235	48
Bun7 N	3815	645031.3	602319.0		
Bun7x N	3855	645020.9	602357.6	275	56
Bun8 S	3580	645091.6	602091.9	660	48/45*
Bun8 N	4240	644919.5	602728.9		
Bun9 S	4020	644977.5	602516.7	220	45
Bun9 N	4240	644919.5	602728.9		
Bun10 S	1965	645508.9	600531.8	130	27
Bun10 N	2095	645475.2	600657.3		

* 48 electrodes for each roll-along spread, excluding the final spread, which used 45.

4.1.4. Measurement Parameters

Table 4 details the type of measurement and array configuration used for each profile measured.

Table 4: Profile ID, measurement type and electrode array configuration used for each profile.

Profile	*ID*	*Measurement Type*	*Array*
Bun1	Bun1	ERT	Schlumberger
	Bun1b	ERT	Wenner Alpha
	Bun1c	ERT	Dipole-Dipole overlap
Bun2	Bun2	ERT	Schlumberger
	Bun2b	ERT	Wenner Alpha
	Bun2c	ERT	Dipole-Dipole overlap
Bun3	Bun3	ERT	Schlumberger
	Bun3b	ERT	Wenner Alpha
	Bun3c	ERT	Dipole-Dipole overlap

Bun4	Bun4	ERT	Schlumberger
	Bun4b	ERT	Wenner Alpha
	Bun4c	ERT	Dipole-Dipole overlap
Bun5	Bun5	ERT	Schlumberger
	Bun5b	ERT	Wenner Alpha
	Bun5c	ERT	Dipole-Dipole overlap
Bun6	Bun6	ERT	Schlumberger
	Bun6b	ERT	Wenner Alpha
	Bun6c	ERT	Dipole-Dipole overlap
Bun7x	Bun7	ERT	Schlumberger
Bun7	Bun7b	ERT	Wenner Alpha
	Bun7c	ERT	Dipole-Dipole overlap
	Bun7a	ERT	Schlumberger
Bun8	Bun8	ERT roll-along	Schlumberger
Bun9	Bun9	ERT	Schlumberger
	Bun9b	ERT	Wenner Alpha
	Bun9c	ERT	Dipole-Dipole overlap
Bun10	Bun10	ERT	Schlumberger
	Bun10a	ERT	Schlumberger
	Bun10d	ERT	Schlumberger
	Bun10e	ERT	Schlumberger
	Bun10b	ERT	Wenner Alpha
	Bun10c	ERT	Dipole-Dipole overlap
	Bun10f	ERT & IP	Wenner Alpha (high power)

Table 5 specifies the parameters used for each measurement.

Table 5: ERT/IP measurement parameters used for the survey.

Measurement method	2D-Multicable
Potential	10 mV / 100 mV *
Electrode spacing	5 m
Zone shape	full
Pulse length	0.3 s / 0.5 s *

IP	None / full decay 2500 ms, 20 windows *

* For Bun10f only (ERT & IP)

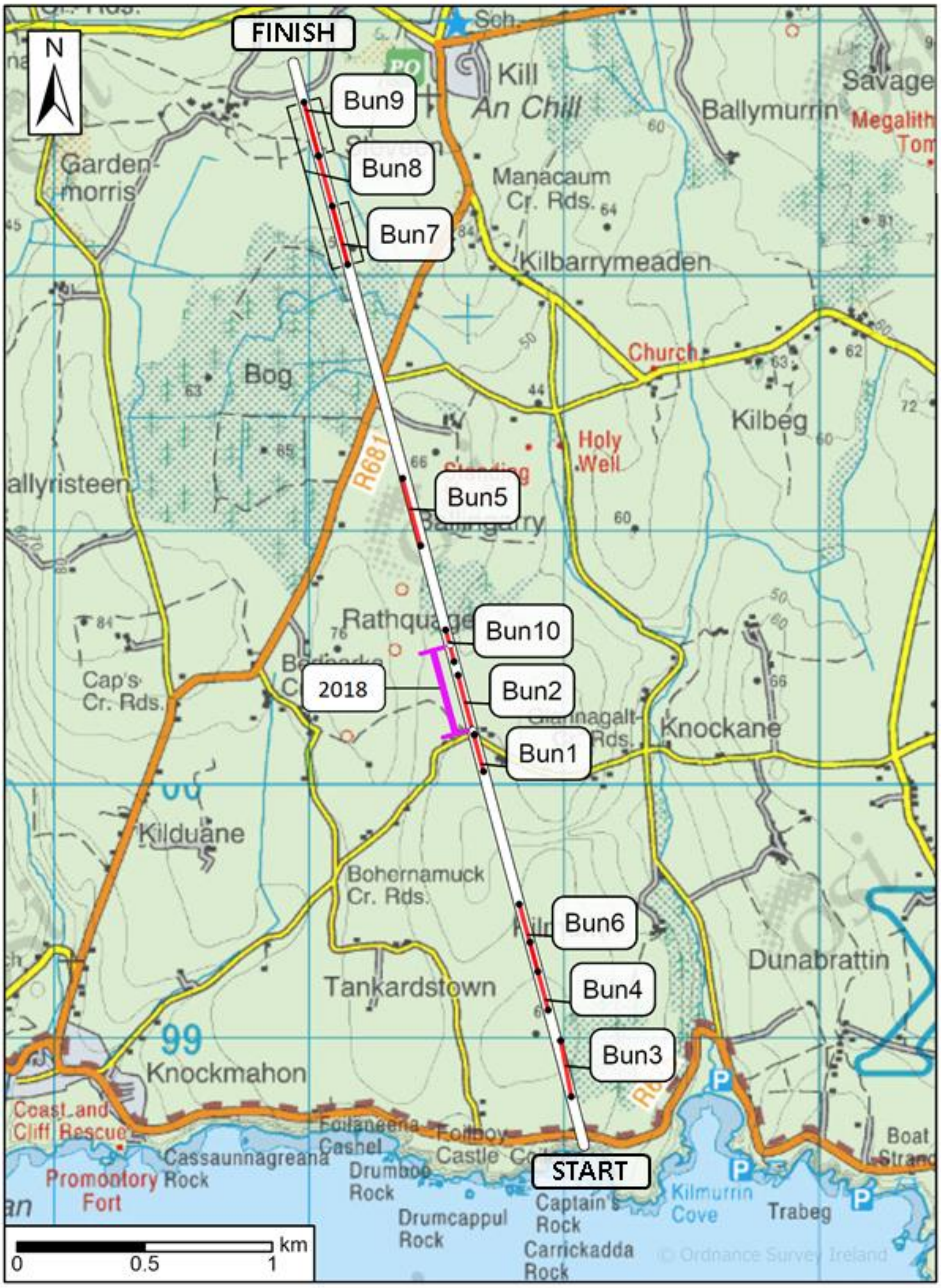

Figure 8: ERT Profiles (red) measured in this survey (2021) along the Waterford test line (white). The purple line illustrates the extent of the ERT profile measured (on the test line) in 2018.

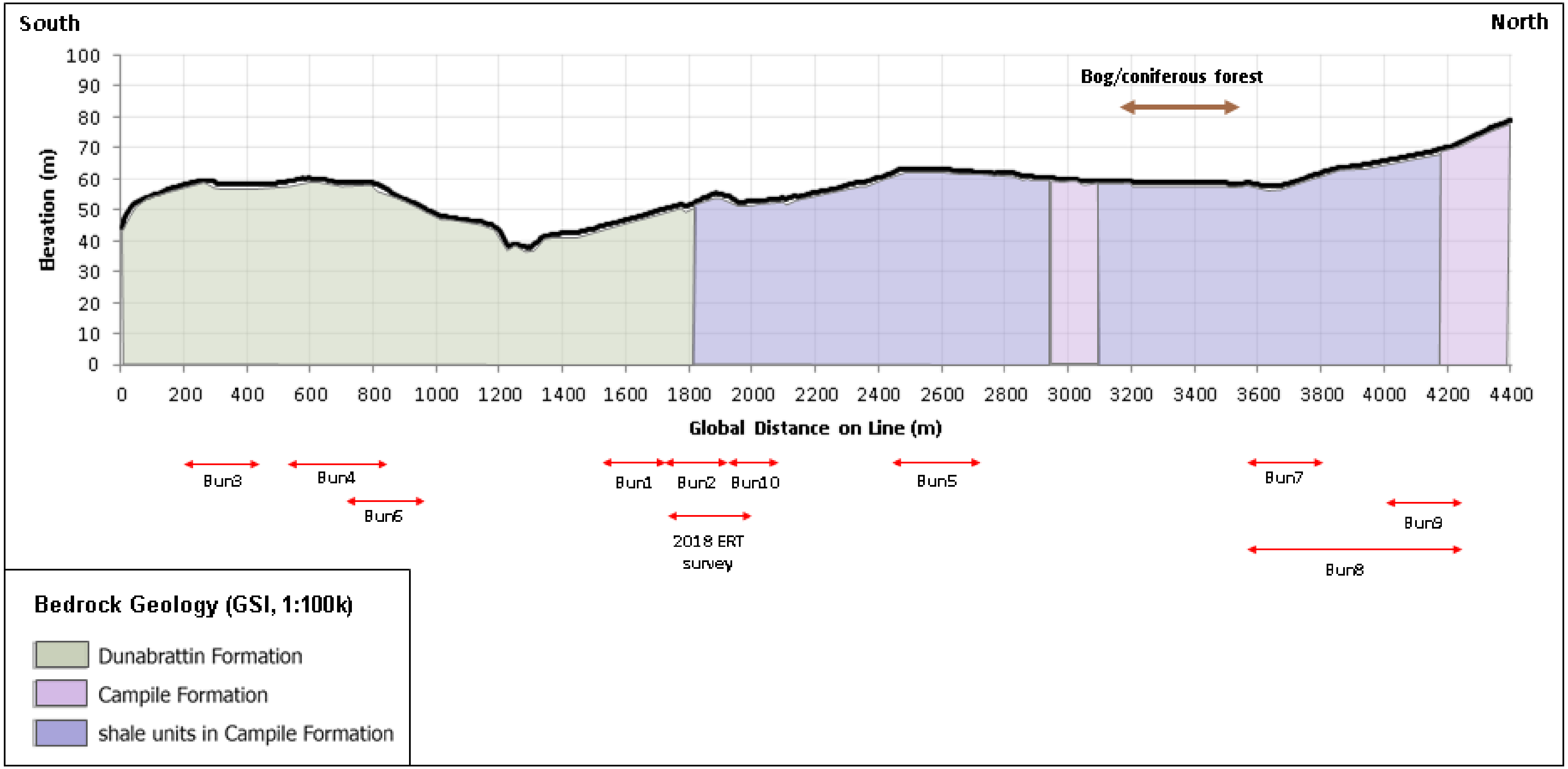

Figure 9: Measured resistivity profile locations, including that of the previous (2018) ground ERT survey, displayed with topography and underlying bedrock geology (from GSI 1:100K Bedrock Geology map).

4.2. Data Processing and Presentation

4.2.1. ERT Inversion Modelling

2-D inversion modelling of ERT data was carried out using ***Res2Dinvx64***, version 4.00 for Windows (© 1995-2011 Geotomo Software). Erroneous apparent-resistivity data points were deleted manually within the programme prior to inversion. Inverse modelled sections were exported as .INV files and manually formatted in Microsoft Excel (© 2010 Microsoft Corporation) as .XYZ files for import into a Geosoft database (see below). Elevations along the profiles were extracted from a Digital Elevation Model (DEM) channel included in the airborne EM test line data delivered by the contractor. Data from the EM DEM channel were gridded in Geosoft using the minimum curvature interpolation method with a 5 m cell size, and subsequently resampled to the locations of the ERT profiles and added manually to the ERT data files prior to inversion.

4.2.2. EM Inversion Modelling

Twenty repeat flights flown at 60 m clearance along the test line were inverted (in 1-D) using the ***aempy*** suite of open-source, *python* based EM processing and modelling software tools developed by researchers at the Dublin Institute for Advanced Studies (DIAS) (Kiyan and Rath 2017, Kiyan *et al.*, 2022). 1-D models of resistivity variation with depth are derived at each measurement site independently and are subsequently gridded together to produce 2-D resistivity sections. EM inversion modelling of the Tellus Waterford (WFD) survey block data, using the *aempy* software, is described in detail in Muller and Hodgson (2020). The EM test line data were inverted using the same *aempy* inversion parameters as used for the Waterford (WFD) survey block (see Table 4.1, Muller and Hodgson 2020), with the exception that a 5-fiducial low-pass filter was applied to the flight altimeter data pre-inversion (rather than the 20-fiducial filter used for the WFD block data). No "cleaning" (rejection of poor model solutions) was applied to the EM test line inversions presented here, except, as indicated below, to exclude resistivity values of < 1 Ωm and > 10,000 Ωm.

It is worth noting that the parameters used for the *aempy* EM inversions (particularly the inversion regularisation parameters and the model depth-layering scheme) were selected to ensure stability and continuity of the model solutions across the whole Waterford production block. It is possible (but not yet tested) that better model spatial resolution could be derived from the EM data by using "locally optimised" inversion parameters.

4.2.3. Gridding and Mapping

Outputs of the inversion models were gridded using inverse distance weighted interpolation in *Geosoft Oasis Montaj* software (version 9.10, © 2021 Geosoft Inc.). Airborne EM sections covering the full extent of the on-land portion of the test line were gridded to a depth of 62.62 m below ground level (bgl) with horizontal and vertical cell sizes of 7.2 m and 2 m, respectively (figure B.1).

Airborne EM resistivity model data were also spatially "clipped" to match the extent of each ERT profile (e.g. Bun1, Bun2, etc.) by creating polygon files for each of the profiles and using the Geosoft *Window X,Y to Polygon Mask* function to create subset databases containing EM data corresponding to each ERT profile extent. New depth and resistivity arrays were then created in these databases such that the maximum depths to which EM resistivity data were gridded matched those of the ERT profiles as closely as possible. The maximum depths of each profile are given in table 6. The gridded model data (both ERT and EM) in figures C.1 – C.10 are clipped so that each of the maximum model section depths along a given profile match that of the shallowest section. Airborne EM data were also edited to exclude erroneous resistivity values of < 1 Ωm and > 10,000 Ωm. The ERT and clipped EM sections were gridded using horizontal and vertical cell sizes of 5 m and 2.5 m, respectively, and mapped side-by-side with a vertical exaggeration of 1.

Table 6: Maximum resistivity model section depths (ERT data as collected; EM data clipped to match depth extent of corresponding ERT profile).

Profile	***ERT Array***	***Maximum Depth (m bgl) - ERT***	***Maximum Depth (m bgl) – clipped EM***
Bun1 - Bun9	Schlumberger	45.59	44.70
Bun1 – Bun9 (excl. Bun8)	Wenner Alpha	28.65	29.87
Bun1 – Bun9 (excl. Bun8)	Dipole-Dipole	28.65	29.87
Bun10	Schlumberger	12.44	12.28
Bun10	Wenner Alpha	24.0	23.45
Bun10	Dipole-Dipole	19.78	20.45

5. Results & Discussion

5.1. Interpretation of Subsurface Structures/Features

Table 7: Line number, electrode array configuration and RMS model error (ERT inversion) for each measured profile. Cells are highlighted in colour where the error exceeds 5% (yellow: 5 – 6% error; orange: 6 – 10% error; pink: > 10% error).

Profile	*Geosoft Line*	*Array*	*ERT Inversion File Name*	*RMS Error (%)*
Bun1	L1.1	Schlumberger	no "INV.xyz" file available	1.40
Bun1b	L1.2	Wenner Alpha	bun1b_topo2_INV.xyz	1.52
Bun1c	L1.3	Dipole-Dipole	bun1c_TOPO_RES.xyz	1.06
Bun2	L2.1	Schlumberger	bun2_TOPO_EDITED_INV.xyz	9.93
Bun2b	L2.2	Wenner Alpha	bun2b_TOPO_INV.xyz	6.49
Bun2c	L2.3	Dipole-Dipole	bun2c_TOPO_EDITTED_INV.xyz	19.79
Bun3	L3.1	Schlumberger	bun3_TOPO2_EDITED_INV.xyz	6.08
Bun3b	L3.2	Wenner Alpha	bun3b_TOPO2_EDITED_INV.xyz	2.40
Bun3c	L3.3	Dipole-Dipole	bun3c_TOPO2_INV.xyz	13.95
Bun4	L4.1	Schlumberger	bun4_TOPO2_INV.xyz	1.25
Bun4b	L4.2	Wenner Alpha	bun4b_TOPO2_INV.xyz	1.19
Bun4c	L4.3	Dipole-Dipole	bun4c_TOPO2_INV.xyz	1.85
Bun5	L5.1	Schlumberger	bun5_TOPO2_INV.xyz	1.51
Bun5b	L5.2	Wenner Alpha	bun5b_TOPO2_EDITED_INV.xyz	1.38
Bun5c	L5.3	Dipole-Dipole	bun5c_TOPO2_INV.xyz	1.86
Bun6	L6.1	Schlumberger	bun6_TOPO2_EDITED_INV.xyz	18.24
Bun6b	L6.2	Wenner Alpha	bun6b_TOPO2_EDITTED_INV.xyz	6.70
Bun6c	L6.3	Dipole-Dipole	bun6c_TOPO2_EDITED_INV.xyz	92.56
Bun7	L7.1	Schlumberger	bun7a_TOPO2_EDITED_INV.xyz	4.45
Bun7b	L7.2	Wenner Alpha	bun7b_TOPO2_INV.xyz	2.78
Bun7c	L7.3	Dipole-Dipole	bun7c_TOPO2_EDITED_INV.xyz	21.60
Bun8	L8.1	Schlumberger	bun8_TOPO2_EDITED_INV	5.39
Bun9	L9.1	Schlumberger	bun9_TOPO2_EDITED_INV.xyz	5.35
Bun9b	L9.2	Wenner Alpha	bun9b_TOPO2_EDITEDI_NV.xyz	3.87
Bun9c	L9.3	Dipole-Dipole	bun9c_TOPO2_EDITED2_RES.xyz	24.54
Bun10d	L10.1	Schlumberger	bun10d_TOPO2_EDITED_INV.xyz	9.76
Bun10b	L10.2	Wenner Alpha	bun10b_TOPO2_EDITED_INV.xyz	10.05
Bun10c	L10.3	Dipole-Dipole	bun10c_TOPO2_EDITED_INV.xyz	25.07
Bun10f	L10.4	Wenner Alpha (with IP; high power)	bun10f_TOPO2_EDITED_INV.xyz	9.95

The ERT inversion models were considered to be more appropriate for interpreting the resistivity structure of the subsurface along the Waterford test line due to a higher measurement density than the airborne EM data and a considerable amount of available information on typical resistivity values of Irish subsoils and bedrock lithologies as measured by ERT. It is also noted that ERT surveys are generally better able to determine the resistivity of resistive bodies than EM surveys. The ERT model sections are shown in Appendix A and the electrode array configurations and RMS model errors for each profile are given in table 7 above. In each figure in Appendix A, the left-hand side corresponds to the southern end of the profile.

Bun1: Figures A.1 – A.3.

The bedrock geology along this profile is mapped as the Dunabrattin Formation (laminated shale and siltstone and peperite). The models show relatively conductive bedrock with an approximate resistivity of 280 – 350 Ωm which suggests high shale content. The bedrock-overburden boundary appears to be at about 15 m bgl although bedrock is shallower towards the southern end of the profile where the resistivity exceeds 350 Ωm. According to the GSI Quaternary Sediments map till derived from acidic volcanic rocks is the predominant subsoil type along the profile, however, a localised alluvial deposit is also mapped at the southern end. The moderately less resistive material (approx. 200 – 270 Ωm) in this area of the models (between 1528 – 1560 m), at depths shallower than ~5 m, could correspond to this alluvium. The range of resistivity values observed in the remaining overburden (80 – 170 Ωm) suggests this material is a till, likely water saturated. All three profiles also show a thin (< 3 m) layer of more resistive, likely gravelly, material above the till between 1550 and 1590 m (distance along profile).

Bun2: Figures A.4 – A.6.

According to the GSI bedrock map there is a boundary between two units approximately two thirds of the way into this profile with the southern portion of the profile mapped as the Dunabrattin Formation and the northern third mapped as “Shale units in the Campile Formation.” When interpreting the models, it should be noted that the RMS error exceeds 5% for the Schlumberger and Wenner arrays, and is almost 20% for the dipole-dipole array. As in Bun1, the conductive (< 100 Ωm) till unit can be distinguished to the south (in the depth range 3 – 10 m) and there are shallow pockets of gravelly material near the surface, overlying the till. Typical bedrock resistivities appear to be between 130 and 250 Ωm and all of the profiles suggest there is more resistive bedrock in the centre of the profile but the change in resistivity is not sharp nor is the boundary well defined.

Bun3: Figures A.7 – A.9.

The mapped bedrock geology of Bun3 and Bun4 is the same as that of Bun1 and the southern half of Bun2 (Dunabrattin Formation) however the former two profiles exhibit much higher bedrock resistivities (> 700 Ωm) implying a change in bedrock type, perhaps to the felsic (rhyolitic) volcanics of the Campile Formation. All three models show a conductive (approx. 150 – 200 Ωm) till unit to a typical depth of about 10 m overlying a transition zone in which resistivities increase with depth and which may be interpreted as a weathered rock layer (250 – 400 Ωm). Deeper intact bedrock resistivities range from 650 to > 2000 Ωm and all three models show a less resistive, vertically-oriented region in the centre of the profile.

Bun4: Figures A.10 – A.14.

The resistivity values observed in the southern half of Bun4 are also high relative to Bun1 and 2, with typical values ranging from 400 to 1100 Ωm, potentially indicative of felsic volcanic bedrock. In this profile, however, the overburden cannot be easily distinguished, and the low-resistivity layer observed in profiles Bun1, Bun2 and Bun3, interpreted as till, is absent. All three models have a more resistive region to the south, while lower resistivity values of 200 – 500 Ωm are observed in the northernmost half of the profile. The models generated to give the lowest RMS errors (figures A.10, A.12 and A.14) all show a distinct, small sub-circular highly-conductive feature at approximately 700 m distance on the profile. A number of anomalously low apparent-resistivity values were edited out of the recorded dataset manually prior to inversion in an attempt to remove what was thought to be an artefact in the data, but the feature remains in the models (figures A.11 and A.13). The sub-circular form and very-low resistivity of the feature suggests it might be man-made in origin, rather than geological, for example a buried metal pipeline or a gravel-filled drain constructed through the middle of the field. The more extensive region of lower resistivity material (200 – 500 Ωm) observed below and to the north of the conductive, sub-circular feature suggests the possibility of more shaley material present in the subsurface at this point.

Bun5: Figures A.15 – A.17.

The shallow subsurface of this profile features pockets of resistive material varying from around 400 Ωm to > 1000 Ωm in places which could be gravelly subsoil containing coarse, resistive (perhaps felsic volcanic) material. The bedrock geology is mapped as "shale units in the Campile Formation" which is consistent with the resistivity values around 300 Ωm. A more resistive body (600 – 1000 Ωm) lies north of the centre of the profile which could be interpreted as felsic volcanic rock. There is also a very resistive body present in all three models at the northern end of the profile at approximately 18-20 m depth bgl, north of what looks to be a weathered fault zone located between 2365 – 2640 m. Overburden resistivities are quite varied but the depth to bedrock can still be estimated to be, on average, about 20 m.

Bun6: Figures A.18 – A.20.

The high RMS errors for the Bun6 models, particularly the dipole-dipole recording, suggest possible measurement errors. Following data collection on the last profile of the day (the dipole-dipole array, with very noisy data observed in the ARES II QC display during recording), one of the seven multi-electrode cables was retired on suspicion of having been damaged. Bun6b (Wenner array) has the lowest RMS error (6.7%) and appears to agree roughly with Bun6 (Schlumberger array) but both must be interpreted with caution. Both sections show a resistive body (1000 – 1700 Ωm) in the centre of the profile at approximately 15 m bgl, separated from a shallower resistor to the north by a much more conductive zone. Bedrock resistivities elsewhere are typically 300 – 500 Ωm. The bedrock geology is mapped as the Dunabrattin Formation (laminated shale, siltstone and peperite) which likely corresponds to the 300 – 500 Ωm resistivity values imaged across much of the profile, however, the 1000 – 1700 Ωm resistors suggest there could also be felsic volcanic rocks present.

Bun7: Figures A.21 – A.23.

The bedrock underlying Bun7 is interpreted as approximately 17 – 20 m bgl and is more uniform than many of the other profiles along the line, with a typical resistivity of 400 – 500 Ωm for the deeper, more intact rock, suggesting it is a fine-grained and perhaps shaley sedimentary rock. The overlying subsoil appears to contain pockets of more conductive material (≤ 100 Ωm) but otherwise has a resistivity of about 100 – 150 Ωm. The subsoil is likely a glacial till with higher clay content interpreted as being present in these conductive regions. Bun7c (dipole-dipole) shows two highly resistive zones within the bedrock and a more uneven top-of-bedrock surface but the model has a significantly higher RMS error than those corresponding to the Schlumberger and Wenner arrays.

Bun8: Figure A.24.

Bun8 is a continuation of Bun7 in a northerly direction. Like Bun7, it features a relatively deep (15 – 20 m) overburden unit, with a typical resistivity between 100 and 180 Ωm and with pockets of more conductive material. The bedrock towards the southern end of the profile has a resistivity of about 450 – 550 Ωm with a much more resistive region (> 1000 Ωm) around 3780 m on the profile, the beginning of which can also be seen on the northern end of Bun7 (figure A.21). North of the resistive region at 3780 m there is a more conductive region in the bedrock, at 3830 m, which could be a geological boundary or fault zone. There is a change in lithology mapped at approximately 4180 m in the GSI 1:100K bedrock map, however, given the scarcity of bedrock outcrops in the area it is possible that this boundary occurs further to the south and corresponds with the conductive bedrock zone observed at 3830 m. Further north of 3830 m, the typical bedrock resistivity appears to increase to 600 – 800 Ω m. The deep conductive overburden material and sudden increase in depth-to-bedrock at 4080 m coincide with a deep ditch with flowing water and a gravel road observed in the field.

Bun9: Figures A.25 – A.27.

Bun9 is the northernmost portion of Bun8. The deep, conductive overburden at the location of the ditch can be seen again, this time at the southern end of the profile. The bedrock elsewhere is around 8 – 12 m bgl, becoming even shallower towards the north, and exhibits resistivity values between 500 and 1000 Ωm. The bedrock geology in the northernmost 60 m (approx.) is mapped (GSI 1:100K bedrock map) as the Campile Formation (rhyolitic volcanics, grey and brown slates) which is compatible with the resistivity range observed, however, as previously mentioned it is possible this geological unit extends further south based on the resistivities. The overburden till is quite conductive and has an average resistivity of about 100 Ωm, and there appears to be a thin more resistive unit overlying the till in the centre of the profile which could be a dry, gravelly material.

Bun10: Figures A.28 – A.31.

The four models for Bun10 have an RMS error of 9.8% or greater and during the data collection negative apparent resistivity responses which coincided with very strong positive (+ 60%) induced polarization (IP) responses were observed, as were negative IP responses which coincided with apparent resistivities of approximately 100 Ωm. The models show a resistive (≥ 500 Ωm) unit approximately 5 m thick overlying significantly more conductive material. The dipole-dipole (figure A.30) and high-power Wenner (figure A.31) models image a deep resistive feature in the bottom right-hand corner of the sections, however, this high-amplitude anomaly appears at a different distance along each of the profiles (approx. 2045 m in Bun10c (dipole-dipole) and 2030 m in Bun10f (high-power Wenner)) and within a different range of resistivity values (1000 – 3000 Ωm and 2000 – 6000 Ωm, respectively). Thus, this high-amplitude anomaly could potentially be an artefact.

5.2. Comparing ERT Array Configurations

There is generally very good agreement between the models produced for the Schlumberger and Wenner array data, and in some cases also the dipole-dipole data. The RMS error is lowest for the Wenner models seven times out of nine, however, that of the Schlumberger model is usually very close behind. As can be seen in table 7 the dipole-dipole array model errors may be significantly higher. Comparing the appearance of features picked out by each method, the Wenner models tend to show quite uniform bedrock with flatter sub-horizontal layer boundaries, whereas the dipole-dipole models often depict an uneven top-of-bedrock surface and more lateral variation within the bedrock itself. Conductive and resistive features tend to be characterised by shorter lateral extent along the profiles or may be laterally offset in the dipole-dipole models relative to the Schlumberger and Wenner models. In Bun9, in one example, the depth to bedrock decreases sharply at the same location along the line in the Wenner and Schlumberger models (at around 4070 m on the profile, figures A.25 and A.26), while in the dipole-dipole model the steep 'jump' appears to occur further to the north (at around 4090 m, figure A.27).

All three models successfully pick out thin resistive layers near the surface of the ground, which are interpreted as gravelly material, with almost identical ranges of resistivity values. Where a till unit is identified, the three array types tend to pick it out successfully with similar ranges of resistivity values and with more conductive pockets within the till identified in the same places. In some cases, the depths at which features are observed differ between the models. In Bun3, for example, the overburden layer appears to be thicker in the Schlumberger model (figure A.7), in Bun5, the deep resistive feature to the north is deeper in the Schlumberger model (figure A.15), and in Bun7 the overburden appears thinner in the dipole-dipole model (figure A.23).

In general, the ranges of resistivity values observed in all three models are very similar, and where they differ it is often due to high- and/or low-amplitude anomalies observed in one model and not in the others. Profiles where the models differ significantly are those with higher RMS errors across the board. The Schlumberger array seems to be a reliable option given the set of measurement parameters used in this survey, as the models produced and the respective RMS errors are in many cases near-identical to those of the Wenner array and the array configuration appears to be more sensitive to the lateral variations that are observed in the dipole-dipole models than the Wenner array. The models produced from Schlumberger array data also imaged the subsurface to a greater depth than the Wenner and dipole-dipole models for a given profile length on all but one occasion (see table 6).

5.3. ERT v. Airborne EM Resistivity Data

Figure B.1 (appendix B) shows 20 airborne EM inversion models. The data cover the full extent of the on-land portion of the Waterford test line and were collected from individual flights in four different years, all flown at the same nominal 60 m ground clearance. The model sections are coloured using the same range of values on a linear scale and have a vertical exaggeration of 1.5. The maximum model depth in the sections is 62.62 m.

A general pattern can be observed across all of the 20 models in figure B.1. There is a highly resistive region at the southern end of the test line and another at the northern end, although, at the northern end the resistivities are not quite as high and the anomalies not as extensive and continuous in some models compared to others. A number of resistive bodies are also found north of the centre of the line, however, these resistive features are less distinct (compared with the southern and northern resistive regions), as there is less of a resistivity contrast, and are more obviously present on some lines than others. North of both the southern and central resistive regions, are two conductive regions. The low resistivity anomalies in the two conductive regions are observed to continue deep into the subsurface and beneath more resistive units, suggesting they correspond to conductive bedrock rather than particularly thick till deposits.

Two airborne EM models that are notably different in places, namely L2060000.19 and L2060011.21, were chosen for comparison with the ground ERT modelled sections (Schlumberger, Wenner and dipole-dipole). In figure B.2 the EM inversion models corresponding to lines L2060000.19 and L2060011.21 are compared to the ERT modelled sections for the Schlumberger array data (all profiles, from Bun3 in the south to Bun8 in the north, excluding Bun1, joined together). Note that the EM sections in figure B.2 have not been clipped to match the different ERT section depth extents along the lines, nor have the EM data been cleaned to exclude resistivities < 1 Ωm and > 10,000 Ωm as per section 4.2.3. At first glance the model outputs of the two methods appear to agree relatively well, with the overall pattern of resistive and conductive regions along the test line present in each of the three lines, however, some notable differences are observed. Along Bun4, for example, both EM models image the large resistive body occupying much of the southern half of the ERT profile as well as the resistor at the northernmost end, however, the shallow resistor located just north of the middle of the ERT model is not observed in either of the EM models.

In Bun2 a sub-vertical resistive feature separating two conductors is observed in the ERT model. The L2060011.21 EM model images a conductive body underlying a thin, more resistive unit as in the ERT model but does not show the sub-vertical resistive feature, while in the L2060000.19 EM model the thin, shallow unit appears to be more conductive than the body lying beneath it.

Differences between the ERT and EM model sections along Bun5 illustrate the poorer resolution of lateral inhomogeneities and very shallow features in the EM models. The ERT and EM models both image a resistive body north of the centre of the profile, however, neither of the EM models image the more conductive, sub-vertical feature splitting this resistor, nor do they show pockets of resistive material in the shallow subsurface as in the ERT model.

The EM model data were clipped to match the lateral and depth extents of the ERT models and edited to exclude data < 1 Ωm and > 10,000 Ωm, and both ERT and EM model data were gridded using an Inverse Distance Weighted algorithm with cell dimensions of 5 m x 2.5 m (horizontal x vertical) (Section 4.2.3). The resistivity cross-sections are presented and compared in figures C.1 – C.10 and summary statistics (of the original inversion model data, not the gridded data sections) are given in tables C.1 and C.2 (Appendix C). The ratios of mean EM to mean ERT resistivities for each profile are given in table 8 below. It should be noted that the summary statistics in tables 8, C.1 and C.2 are based on all of the model data for each ERT array and the EM data that matches the extent (lateral and depth) of these ERT model sections, whereas in figures C.1 – C.10 all of the model sections have been clipped to the maximum depth of the **shallowest** section to facilitate a visual comparison.

Table 8 (a – f): Mean resistivities (Ωm) and EM:ERT ratios for clipped and edited airborne EM [L2060000.19 and L2060011.21] models and ERT [Schlumberger (S), Wenner (W) and dipole-dipole (D)] models (see tables C.1 and C.2). Statistics are based on the original inversion model data. Cross-sections are shown in figures C.1 – C.10, Appendix C.

(a)	**EM L2060000.19**	**ERT (S)**	**EM/ERT**
Bun1	-	-	-
Bun2	269.8	217.9	1.2
Bun3	1014.6	549.5	1.8
Bun4	791.3	851.0	0.9
Bun5	461.2	533.4	0.9
Bun6	453.1	619.6	0.7
Bun7	285.3	290.3	1.0
Bun8	337.5	393.0	0.9
Bun9	443.7	592.8	0.7

(b)	**EM L2060011.21**	**ERT (S)**	**EM/ERT**
Bun1	-	-	-
Bun2	272.7	217.9	1.3
Bun3	853.0	549.5	1.6
Bun4	1196.9	851.0	1.4
Bun5	509.0	533.4	1.0
Bun6	568.2	619.6	0.9
Bun7	317.1	290.3	1.1
Bun8	340.8	393.0	0.9
Bun9	432.3	592.8	0.7

Bun10	153.4	370.3	0.4

Bun10	154.2	370.3	0.4

(c)	EM L2060000.19	ERT (W)	EM/ERT
Bun1	179.3	244.7	0.7
Bun2	257.6	216.7	1.2
Bun3	821.9	506.6	1.6
Bun4	710.1	851.9	0.8
Bun5	466.9	548.2	0.9
Bun6	445.5	774.6	0.6
Bun7	263.7	247.6	1.1
Bun8	-	-	-
Bun9	405.0	435.6	0.9
Bun10	179.1	332.6	0.5

(d)	EM L2060011.21	ERT (W)	EM/ERT
Bun1	168.8	244.7	0.7
Bun2	205.2	216.7	0.9
Bun3	630.6	506.6	1.2
Bun4	1215.7	851.9	1.4
Bun5	414.8	548.2	0.8
Bun6	479.3	774.6	0.6
Bun7	241.7	247.6	1.0
Bun8	-	-	-
Bun9	327.4	435.6	0.8
Bun10	170.4	332.6	0.5

(e)	EM L2060000.19	ERT (D)	EM/ERT
Bun1	179.3	281.2	0.6
Bun2	257.6	179.7	1.4
Bun3	821.9	2832.5	0.3
Bun4	710.1	904.6	0.8
Bun5	466.9	651.1	0.7
Bun6	445.5	657.6	0.7
Bun7	263.7	407.7	0.6
Bun8	-	-	-
Bun9	405.0	445.0	0.9
Bun10	173.9	574.8	0.3

(f)	EM L2060011.21	ERT (D)	EM/ERT
Bun1	168.8	281.2	0.6
Bun2	205.2	179.7	1.1
Bun3	630.6	2832.5	0.2
Bun4	1215.7	904.6	1.3
Bun5	414.8	651.1	0.6
Bun6	479.3	657.6	0.7
Bun7	241.7	407.7	0.6
Bun8	-	-	-
Bun9	327.4	445.0	0.7
Bun10	162.3	574.8	0.3

The above tables illustrate how the average resistivity values are generally comparable between EM and ERT models and between different flights or ERT array configurations with a few exceptions, notably Bun2, Bun3 and Bun4 (where the EM/ERT ratio is high), and Bun10 (where the EM/ERT ratio is very low). These particular ERT profiles have higher ERT model RMS errors on average (table 7) and, as can be seen in table 8, the two EM models have substantially different mean resistivities for Bun3, so there may be greater uncertainty in the EM measurements/models along the Bun3 portion of the test line. Mean resistivities in the ERT models slightly exceed those in the EM models more often than the contrary (i.e., the EM/ERT ratio is more often less than 1). There does not appear to be any significant correlation between the EM/ERT ratio and how resistive (or conductive) the ground is along a given profile (figure B.2 for reference), nor the underlying (mapped) geology. It is noted, however, that the resolution (measurement densities) and methods of inversion modelling differ between the EM and ERT data, and many of the model sections feature a wide range of resistivity values. Thus, a comparison of only the mean EM and ERT resistivities (or ratios of such means) along the profiles is likely to be of limited value when assessing the compatibility of the respective methods.

Looking at the model sections side-by-side (figures C.1 – C.10), while the ranges of resistivity values may be comparable, the airborne EM and ground ERT methods do not always image the same features in matching locations in the subsurface. In figure C.2, for example, we see two conductive zones either side of the centre of the profile in all three ERT models and the L2060011.21 EM model, however, the conductor to the north is a deep feature in the ERT models but lies close to the surface of the ground above a more resistive body in the L2060011.21 EM model. In figure C.5 not all features present in the three ERT models are found in the EM models, nor are the resistivity values identical, but the main resistive bodies are observed in both the ERT models and the L2060011.21 EM model at similar positions along the profile. In this instance the resistive bodies appear to be imaged at a greater depth in the EM model. The ERT and EM sections in figure C.1 on the other hand bear almost no resemblance to one another, while those in figures C.3 and C.7 are very similar.

Figures 10 – 12 below consider three profiles in which there is good agreement between the airborne EM and ground ERT inversion models. Approximate locations of boundaries between the different geological units present (as the model sections have been interpreted) have been illustrated on the figures as dashed black lines. A 1st vertical derivative convolution filter was applied to the model grids shown in figures 10 – 12 to help define boundaries between resistive and conductive bodies. The 1st vertical derivative grids (shown below the resistivity sections in figures 10 – 12) were smoothed using a 7x7 symmetric convolution filter. Absolute value 1st vertical derivative grids (not shown) were used to aid annotation of the resistivity sections.

Both models in figure 10 resolve three subsurface units. The ERT model resolves a shallow unit boundary (approx. 2 – 8 m bgl) which is not resolved in the EM model. The 1st vertical derivative grid is positive (red) in this uppermost region which implies the resistivity values here are increasing. The resistivities here are low (< 200 Ωm) and there is not a large contrast between this shallow layer and that lying directly below it. A possible interpretation is that the uppermost unit boundary represents the local water table and the material above this boundary is drier and consequently more resistive than that below it. It is worth noting that the uppermost unit boundary in the ERT model is imaged at < 2.5 m below ground level in places, which is less than the vertical cell size that was used to grid the data. Thus, the very shallow zones of increasing resistivity may represent only a single grid node and should be interpreted with caution. There are, however, regions on this profile (and on other profiles) in which this uppermost unit is > 5 m thick, giving greater confidence in its physical significance. Both the ERT and EM models image a moderately conductive (200 – 500 Ωm) unit which is, on average, 10 – 20 m thick in both models, and is found beneath the uppermost unit in the ERT model and at the surface of the EM model. The unit appears to be slightly more resistive in the EM model, although this gradual increase to higher resistivities towards the base of the unit could simply be the result of a smooth model transition and may not have any physical significance.

Considering figure 10 further, both models image a deep resistor (> 800 Ωm) with an upper boundary resolved between 23 m bgl at the southern end of profile (in both models) and 7 – 14 m bgl at the northern end (the greater depth corresponding to the EM model). The ERT model resolves a zone of less resistive material splitting this body whereas it appears continuous in the EM model. In the latter an additional layer boundary underlying this resistor is resolved between > 45 m bgl (in the south) and 30 m bgl in the north. The 1st vertical derivative is negative in this region implying that the resistivity values here are decreasing. The section plan view in the upper right-hand corner of the figure shows a slight offset between the ERT profile and the EM line which may be responsible for some of the variability between the models.

In figure 11, the resistivity values in both sections are very similar, with a slightly higher maximum in the ERT model, and three layer boundaries are resolved in each, this time at comparable depths in contrast to figure 10. The uppermost, near-horizontal boundary appears between 5 – 10 m bgl in both models with an undulating character in the ERT model. The vertical derivatives are positive above this boundary, as in figure 10, this time in the EM model as well as in the ERT model. Pockets of more conductive material appear within the conductive unit lying below the uppermost boundary in the ERT model that are not visible in the EM model, illustrating the potential lower lateral resolution of the latter, however subtle variations in the EM vertical derivative grid are observed in this region. A resistive (> 500 Ωm) body is imaged in the centre of the two models with an upper boundary at approximately 20 m bgl and a transition to lower resistivities is observed around 40 m bgl. The resistor's upper boundary is more uneven in the ERT model and dips more steeply at both ends of the body (southern and northern) compared to the EM model, however, a comparison of figures 11 and 12 suggests that the edges of the ERT model sections are poorly constrained. The

Bun7 profile coincides with the southernmost 235 m of Bun8 (figure 12), as indicated by the red arrow in figure 12. It can be seen clearly in figure 12 that the near-vertical northern boundary of the resistive body appears immediately north of the end of Bun7, while on Bun7 itself, the boundary is located some 25 m to the south of the end of the profile (figure 11). It appears that while the sharp edge of the resistive body is detected at the northern-most end of Bun7, there is not enough data coverage at the end of Bun7 to place the boundary accurately in the subsurface. This discordance or break in the resistive body is also observed in the EM grid, but with a smoother expression.

The 'smoothed out' appearance of subsurface features and less detail in the EM section, due to lower model resolution, is also evident in figure 12 (Bun8). Here, the thickness and resistivity of the uppermost conductive layer are comparable but the deeper resistive unit has a greater average resistivity (approx. 750 Ωm) and is more laterally discontinuous in the ERT model compared to the EM model (550 Ωm). Despite these differences, however, the models are visually similar, the depths of the defined unit boundaries defined are in good agreement, and both vertical derivative grids show a transition to higher resistivities above the uppermost layer boundary and to lower resistivities towards the bottom of the sections.

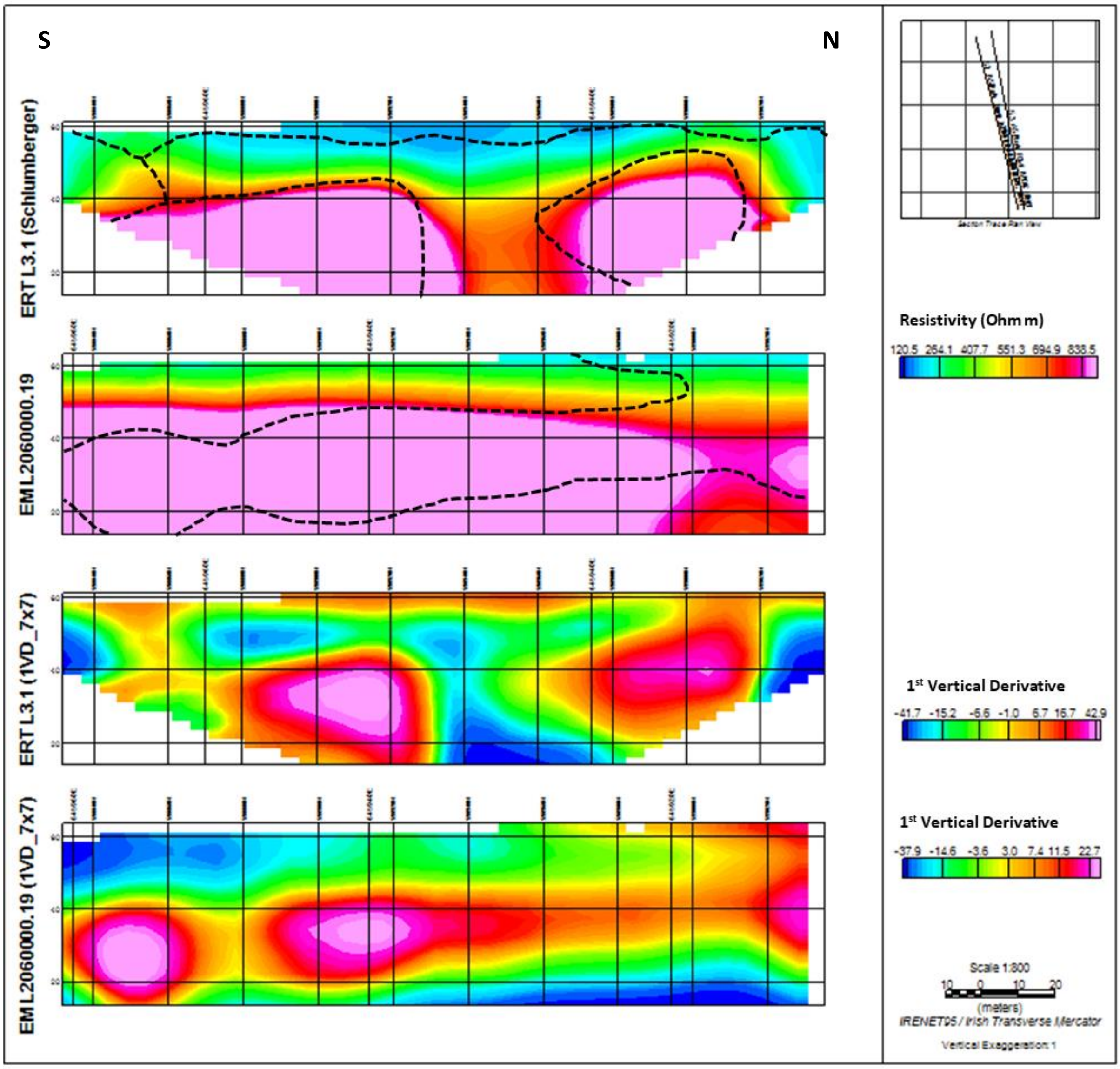

Figure 10: Comparison of clipped and edited EM (L2060000.19) model section and ERT (Schlumberger) section along Bun3 (top). The sections are classified using identical linear colour scales and annotated to show interpreted boundaries (based on 1st vertical derivative absolute value grids) between geological units. 1st vertical derivative grids (not absolute value) are shown beneath the resistivity sections. Note: the derivative grids do not use the same linear colour scale as the resistivity grids.

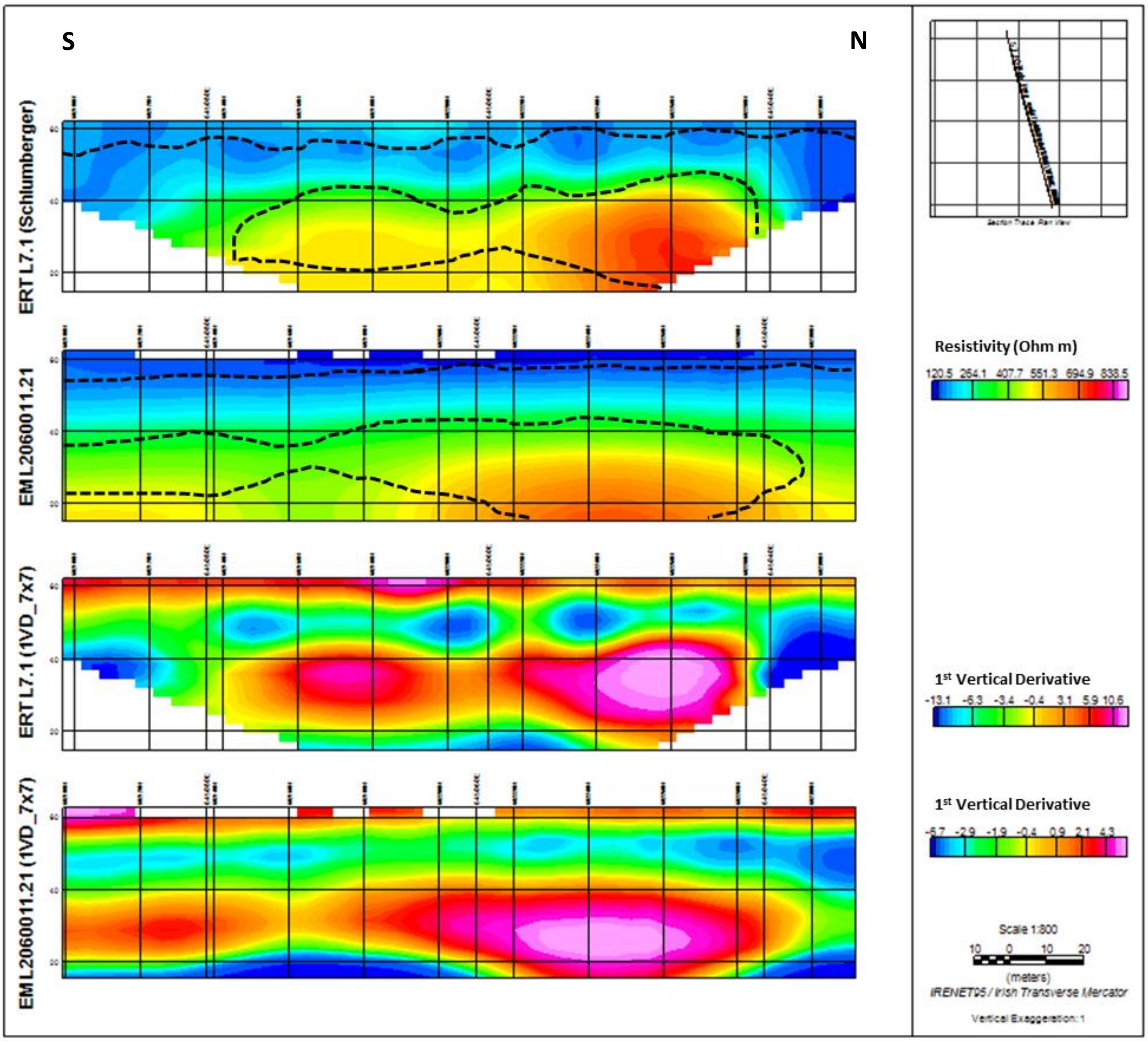

Figure 11: Comparison of clipped and edited EM (L2060011.21) model section and ERT (Schlumberger) section along Bun7 (top). The sections are classified using identical linear colour scales and annotated to show interpreted boundaries (based on 1st vertical derivative absolute value grids) between geological units. 1st vertical derivative grids (not absolute value) are shown beneath the resistivity sections. Note: the derivative grids do not use the same linear colour scale as the resistivity grids.

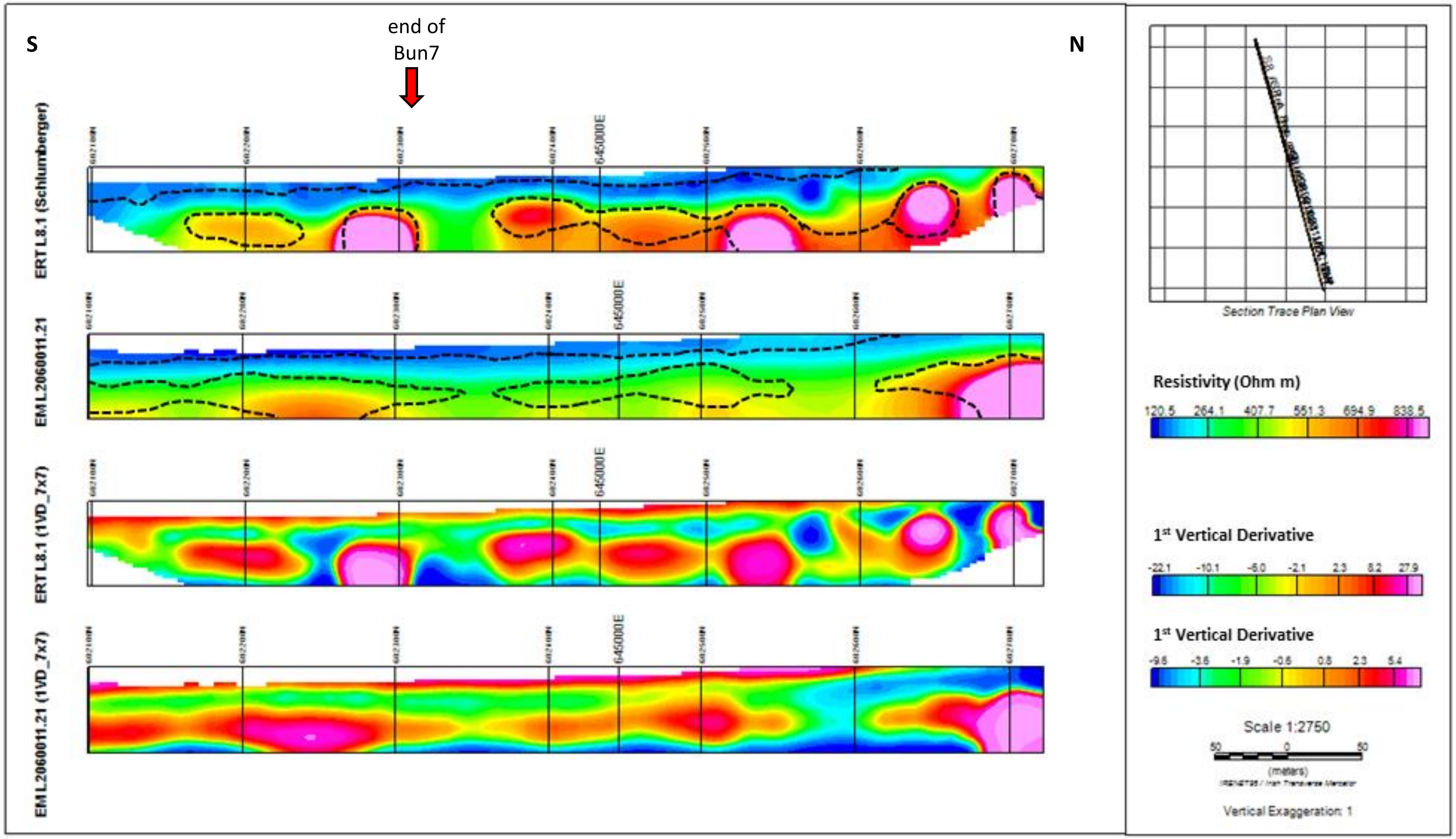

Figure 12: Comparison of clipped and edited EM (L2060011.21) model section and ERT (Schlumberger) section along Bun8 (top). The sections are classified using identical linear colour scales and annotated to show interpreted boundaries (based on 1st vertical derivative absolute value grids) between geological units. 1st vertical derivative grids (not absolute value) are shown beneath the resistivity sections. Note: the derivative grids do not use the same linear colour scale as the resistivity grids.

5.4. Comparing Data from 2018 and 2021

The Waterford test line ERT data from October 2018 were collected using a Wenner array along a line that is coincident with Bun2 and with the southern half of Bun10 from this 2021 ground survey. The 2018 profile was inverse modelled using *Res2Dinv* and is presented in figure 13 below in Geosoft gridded format alongside ERT (Bun2 and Bun10; Wenner array) models from 2021, the EM models (L2060000.19 and L2060011.21; cleaned to exclude data < 1 Ωm and > 10,000 Ωm), and 1st vertical derivative grids (smoothed using a 7x7 symmetric convolution filter) corresponding to each of the sections. All data have been clipped to match the lateral extent of the 2018 ERT profile and the depth extent of the 2018 ERT profile (54.26 m) with the exception of the 2021 ERT data, which are gridded to their maximum depths (28.65 m for Bun2 and 24.0 m for Bun10). The data were gridded using an Inverse Distance Weighted algorithm with cell dimensions of 5 m x 2.5 m (horizontal x vertical).

Comparing the sections in figure 13, it is clear that neither the 2021 ERT data nor the EM data yield an inversion model that matches the 2018 ERT inversion model exactly. With regard to the locations of picked unit boundaries (black dashed lines), there is good agreement between the two ERT models (top) where they coincide. Both image a thin resistive layer at the surface of the section, ranging from 5 – 13 m thick in places, overlying a thicker conductive unit with a range of resistivity values indicative of till or conductive bedrock such as shale, and a deep, more resistive bedrock unit. The upper boundary of the deep resistor appears more uneven in the 2021 model, however, and is imaged at a greater depth in places (particularly in the middle of the profile) in the 2018 model. The resistivities observed in the uppermost layer are also notably higher in the 2018 model compared to the 2021 ERT model. The ERT models differ most significantly in the northern part of the profile (Bun10). Here the 2018 model shows a resistive feature lying beneath the till unit whereas in the 2021 model the resistivity appears to decrease with depth.

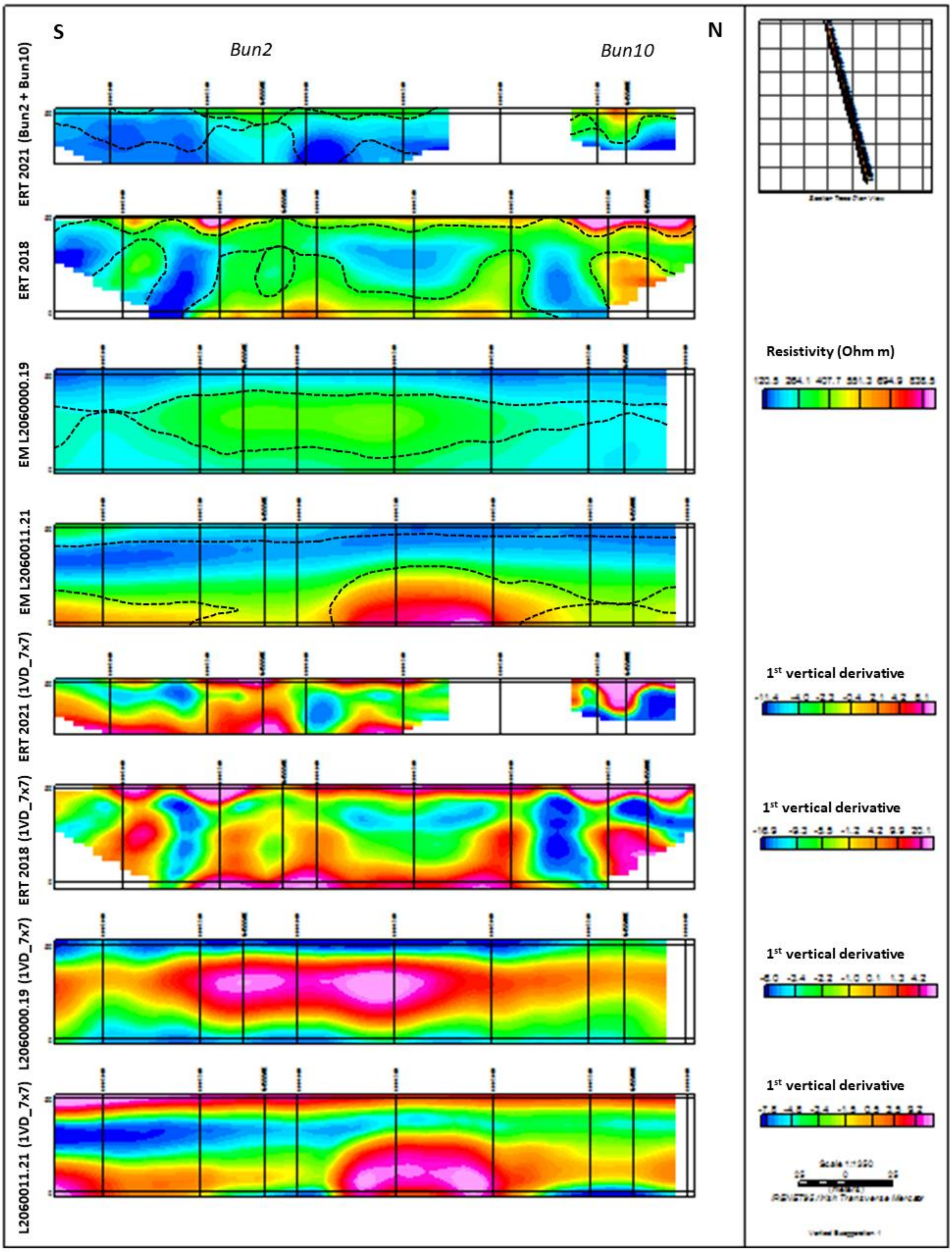

Figure 13: Comparison of resistivity model grids (top) and 1st vertical derivative grids (bottom) of 2021 ERT data (profiles Bun2 and the southern half of Bun10; Wenner array), 2018 ERT data (Wenner array), and EM data (lines L2060000.19 and L2060011.21). The linear colour scale used in the top four resistivity grids is identical to that which is used in figures 10 – 12. Absolute value 1st vertical derivative grids (not shown) were used to aid annotation of the resistivity model grids.

Of the two EM models, L2060011.21 more closely resembles the ERT data. In the L2060011.21 model, a central conductive unit is observed with resistivities comparable to those in the ERT models and there are more resistive layers in L2060011.21 lying above and below this central conductor, as highlighted in the vertical derivative grid. In contrast to the ERT models, however, the deeper resistor becomes shallower in the northern half of L2060011.21 and the uppermost resistor becomes thicker towards the south. The L2060000.19 EM model, unlike the other three, features a relatively resistive body in the centre of the profile at a much shallower depth (10 – 15 m bgl) and with a lower average resistivity (approx. 400 Ωm) than the deep resistors in the other models. Differences in both the vertical and lateral resolution between the EM and ERT datasets are apparent, as variations in thickness are smooth and gradual in the EM models compared to the ERT models, and resistivity contrasts within the subsurface units are better defined in the latter.

This comparison highlights the variability of EM data between different flights as well as the differences between airborne EM and ground ERT data, but also illustrates the potential for ERT data and the resulting resistivity models to vary between successive surveys carried out using near-identical measurement methods and parameters.

6. Conclusions & Recommendations

6.1. Conclusions

6.1.1. Agreement between ERT array configurations

In general, good agreement was observed between array types, particularly the Schlumberger and Wenner arrays, except where the model RMS error for a given profile was high (approximately ≥ 10%). The Wenner array typically had the lowest RMS model error but the Schlumberger was usually very close behind and seems to be a good compromise between the other two arrays (lower % error than dipole-dipole; better at picking out vertical discontinuities/variations in resistivity than Wenner). In some cases, the overburden thickness was greater in the Schlumberger model than the other two arrays, although only by 1 – 2 m. The ERT data collected along profile Bun10 using a Wenner array with a high (100 mV) measurement potential (Bun10f) were comparable to the other Wenner and Schlumberger data for this profile, with all three models appearing visually very similar and having RMS errors between 9.8% and 10.1%.

6.1.2. ERT v. airborne EM inversion models

Comparison of ERT and EM models in which the observed features were similar found that boundaries between distinct units (conductors and resistors) in the subsurface were imaged at very similar depths and generally with comparable resistivities in both models, although in some cases the maximum resistivities of highly resistive bodies in the ERT models exceeded those in the EM models. Except where ERT model RMS errors were particularly high, the range of resistivity values in both models (ERT and EM) were comparable, with ratios of (mean EM resistivity)**:**(mean ERT resistivity) generally falling between 0.7 and 1.25. The model sections along a given profile do not always resemble one another in appearance (e.g., figures C.1, C.6 and C.10), however, there also appeared to be substantial variability between the results of successive ERT surveys and between airborne data collected during different flights and different years (figure 13). Where the sections do appear similar, the resistivity values at which geological boundaries may be interpreted are generally comparable (figures 10 – 12). The resolution of the ERT data was noticeably higher in the shallower subsurface, particularly where thin resistive layers occurred at the surface or where pockets of conductive material occurred within the subsoil.

6.2. Recommendations

6.2.1. Airborne EM data repeatability

It is recommended the repeatability of the airborne EM data between flights and different survey years is investigated to aid assessment of the significance of observed differences between the airborne EM inversion models and the ground ERT inversion models. Good agreement between ERT data collected using three different electrode array configurations gives some confidence in the accuracy of the measurements (although the dipole-dipole models were sometimes quite dissimilar), however, the discrepancy between the ERT data collected near Bun2 in 2018 and the data collected for this survey could suggest there is also some variability inherent in the ground survey data. It would therefore be useful to repeat the ground ERT survey along a number of profiles to assess this variability.

6.2.2. Inverse modelling of Bun10 IP data

The ERT inversion model sections for Bun10 had high RMS errors and were considerably different from the airborne EM models as well as from the ERT survey which used a dipole-dipole array on the same profile. Negative apparent resistivities and negative induced polarization responses were observed during the data collection along this profile. The IP data have not as yet been inverse modelled and are therefore not discussed in this report. It is recommended the IP data be inverted to assist interpretation of the resistivity structure of the subsurface along this portion of the Waterford test line.

References

Beamish, D., Tartaras, E., Suppala, I. and Hautaniemi, H., 2006. JAC Airborne EM software: In: AEM Workshop Hannover 2006 Airborne EM Recent Activities and Future Goals (Extended Abstracts Book).

Copernicus Land Monitoring Service (Copernicus), 2018. CORINE Land Cover 2018. Available at https://land.copernicus.eu/pan-european/corine-land-cover/clc2018. Accessed: 21/10/2021.

Crowley, B. and Ture, M. D., 2018. Geophysics Ground Investigation on Tellus Airborne Testline in Bunmahon, County Waterford, September 2018. Geological Survey Ireland Internal Report.

GF Instruments, s.r.o., Ares II Automatic resistivity and IP System. User manual v. 1.5.

GF Instruments, s.r.o., 2019. Short guide for resistivity and induced polarization tomography. Edition 2019.

Kiyan, D. and Rath, V., 2017. Inverse Methods for Airborne Electromagnetic Data from the Tellus Surveys: The aempy Toolbox. Unpublished report and user manual, Dublin Institute for Advanced Studies, Ireland, March 21, 2017.

Kiyan, D., Rath, V., Muller, M. R., Ture, M. D. and Hodgson, J., 2022. 1-D Inversion of Frequency-Domain Airborne Electromagnetic Data using the *aempy* Toolbox. Accepted, Journal of Applied Geophysics, DOI pending.

Muller, M. R. and Hodgson, J. A., 2020. Tellus Waterford (WFD) Block: *aempy* Electromagnetic Inversion Report. Geological Survey Ireland Report.

Reynolds, J. M., 2011. An Introduction to Applied and Environmental Geophysics, 2nd Edition. New York, NY: Wiley-Blackwell.

Sander Geophysics Ltd (SGL), 2019. Technical Report: Fixed-Wing High-Resolution Aeromagnetic, Gamma-ray Spectrometric and Frequency-Domain Electromagnetic Survey - Tellus A7 Block, Republic of Ireland 2019 - For Geological Survey Ireland.

Ture, M. D. and Hodgson, J. A., 2017. Tellus GTK-FDEM system characteristics and applications. Geological Survey Ireland Report.

Ture, M. D., 2020. Tellus Merge-2019B Airborne Geophysical Technical Report (Operations, Logistics and Data Merging). Geological Survey Ireland Report.

Ture, M. D. and Muller, M. R., 2020. Tellus Interpretation Guide to Airborne Geophysics. Geological Survey Ireland Report.

Appendix A: ERT Resistivity Models (Res2Dinv)

The following sections are oriented South to North (left to right).

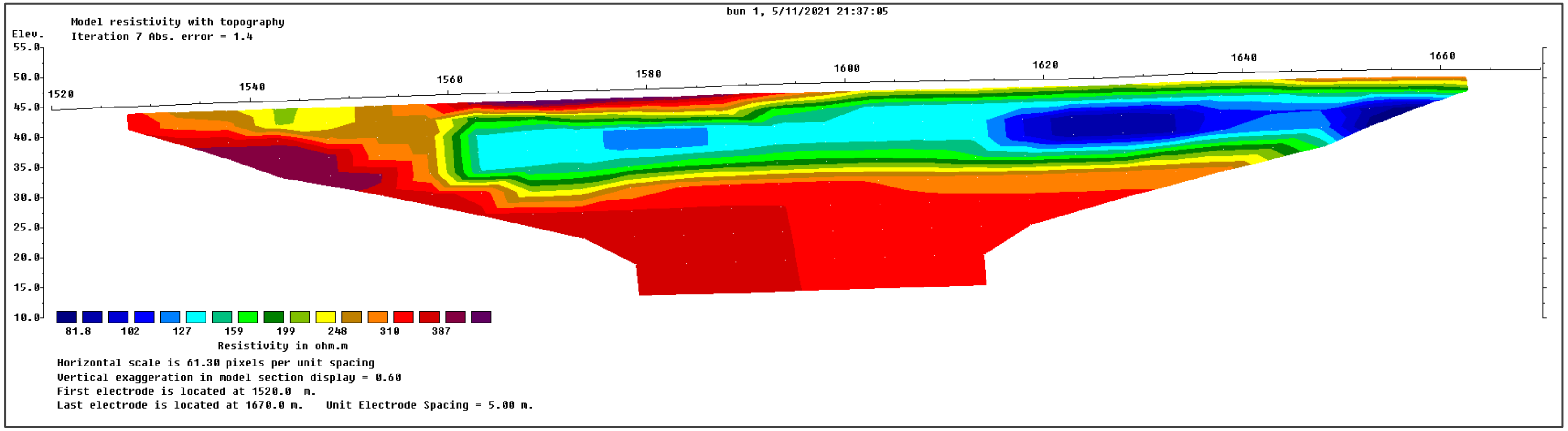

Figure A.1: Bun1 (Schlumberger array).

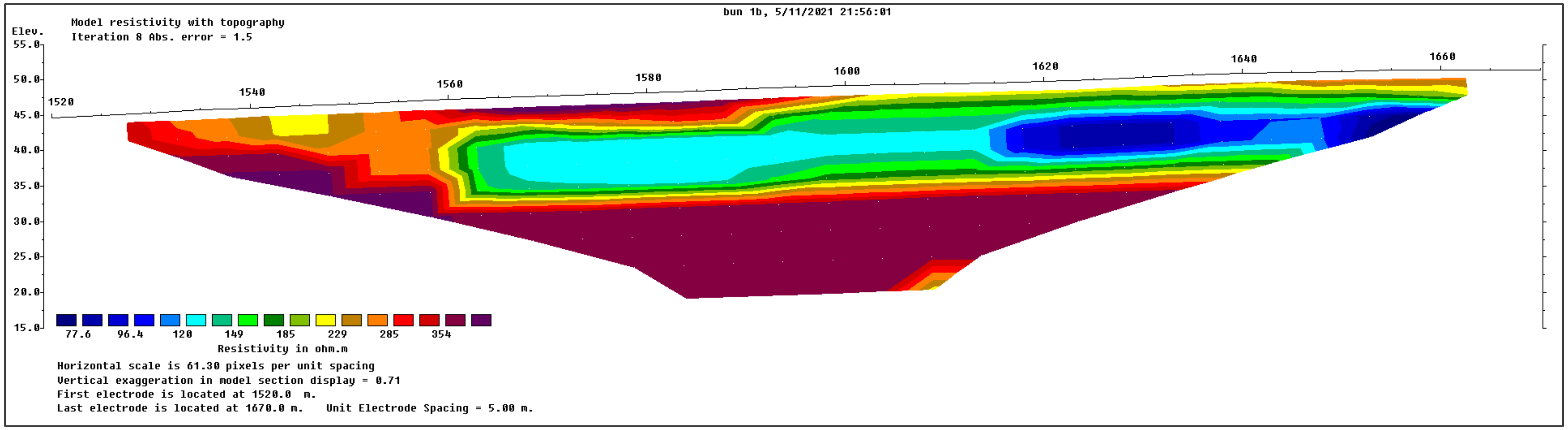

Figure A.2: Bun1b (Wenner array).

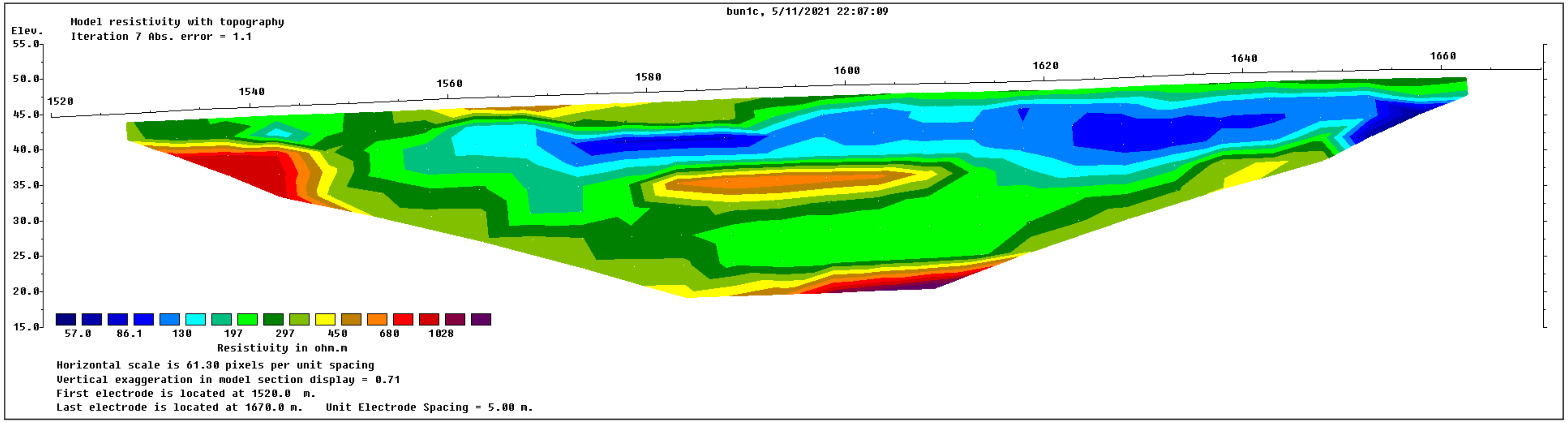

Figure A.3: Bun1c (Dipole-dipole array).

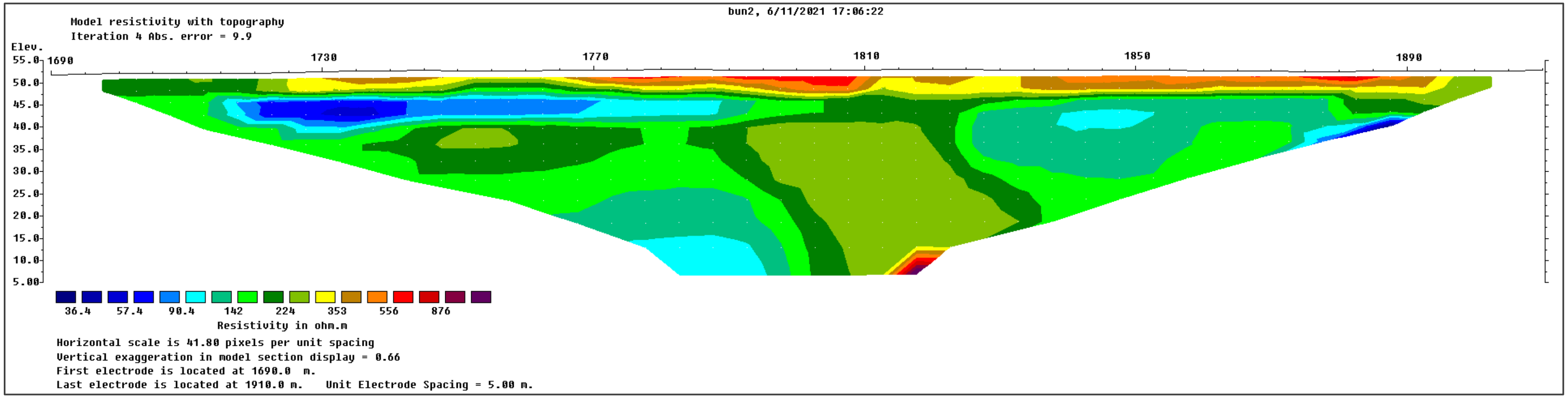

Figure A.4: Bun2 (Schlumberger).

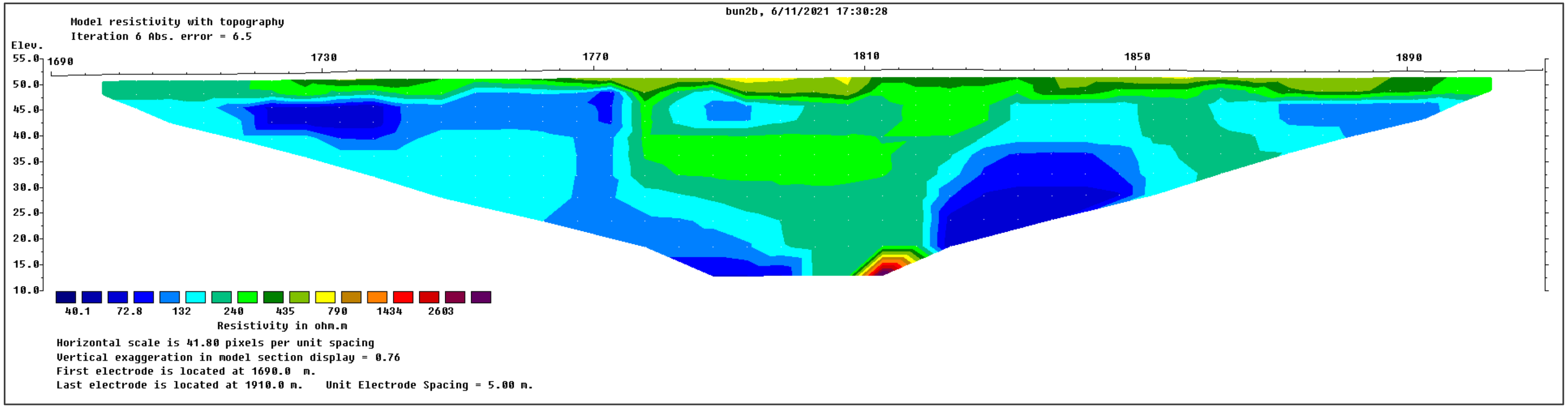

Figure A.5: Bun2b (Wenner).

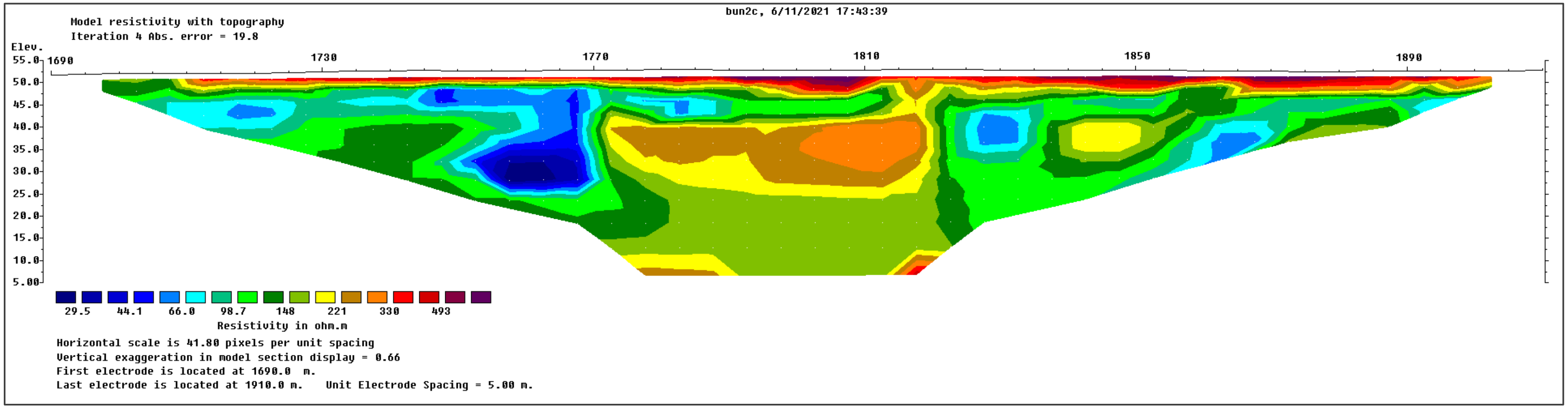

Figure A.6: Bun2c (Dipole-dipole).

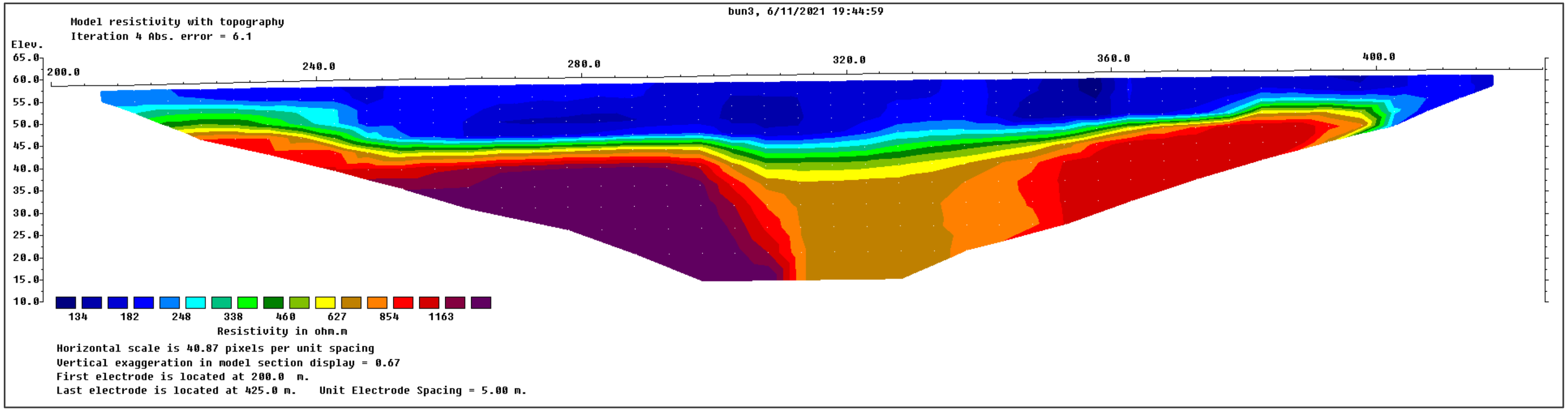

Figure A.7: Bun3 (Schlumberger).

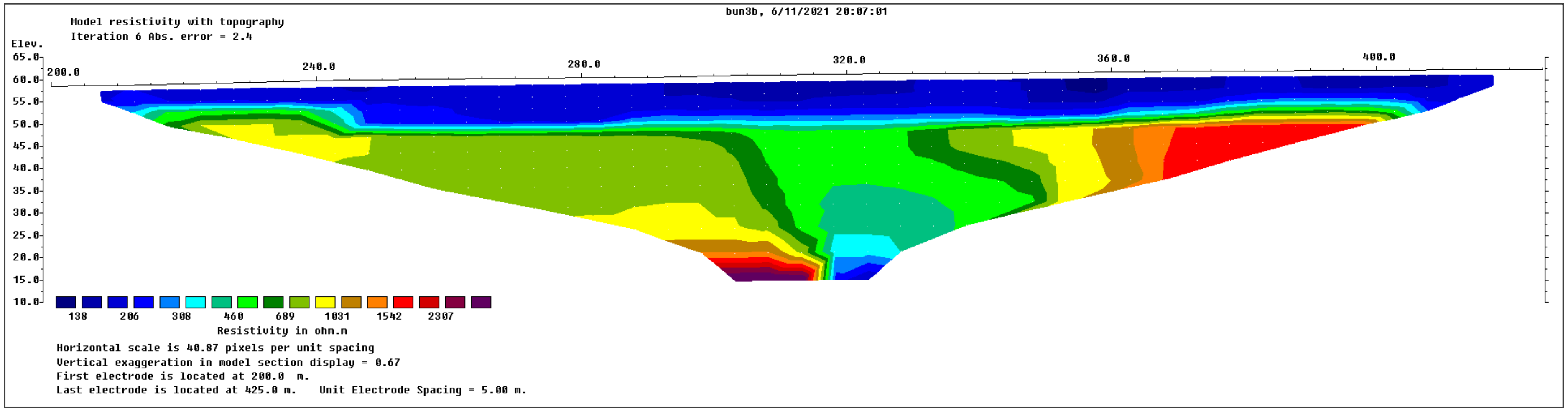

Figure A.8: Bun3b (Wenner).

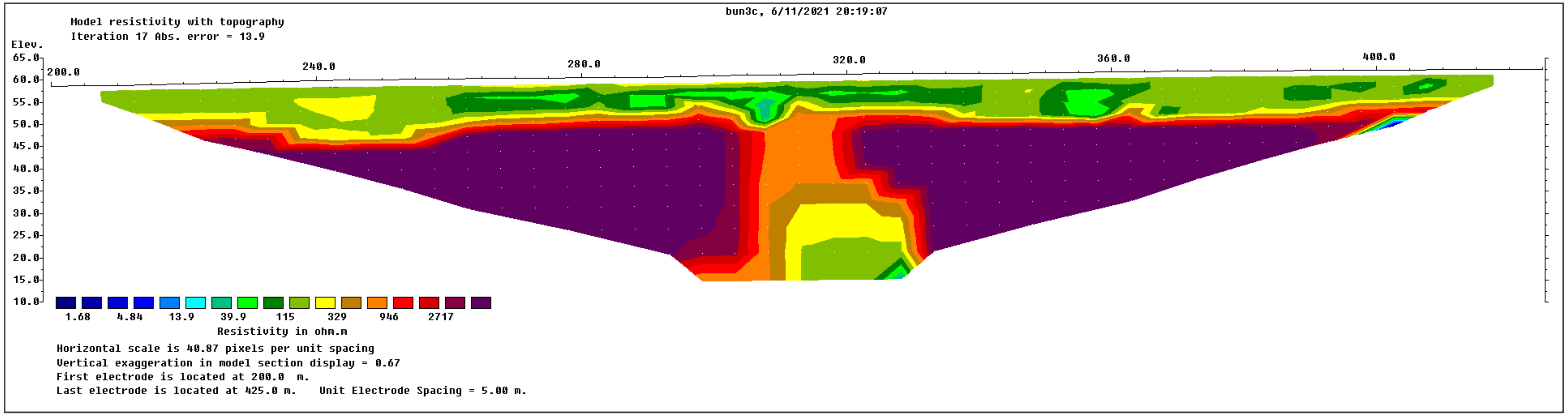

Figure A.9: Bun3c (Dipole-dipole).

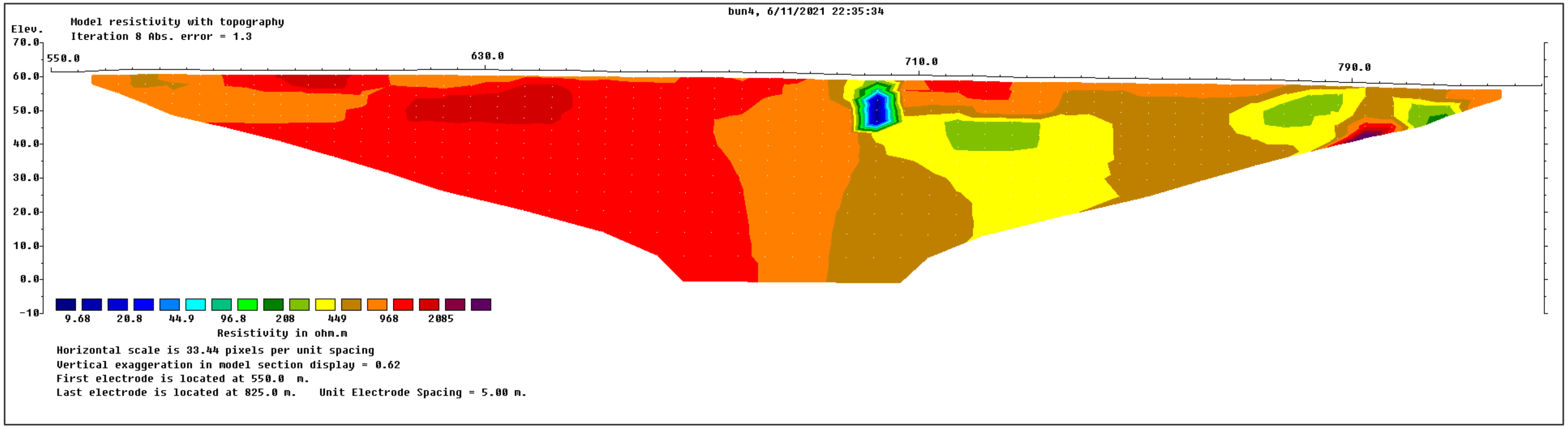

Figure A.10: Bun4 (Schlumberger).

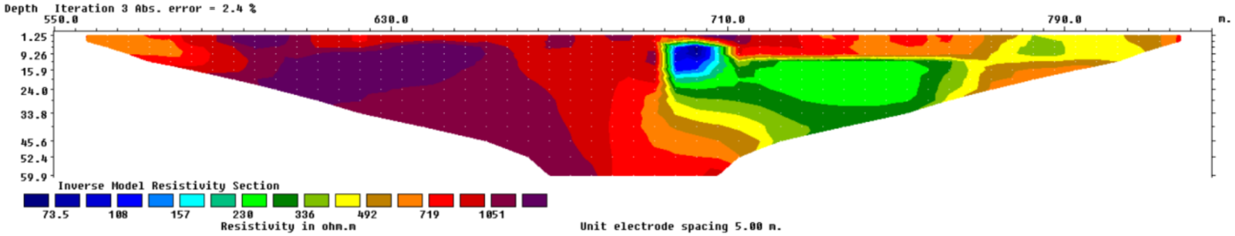

Figure A.11: Bun4 (Schlumberger) edited by deleting points in Res2Dinv. Note no topography in model.

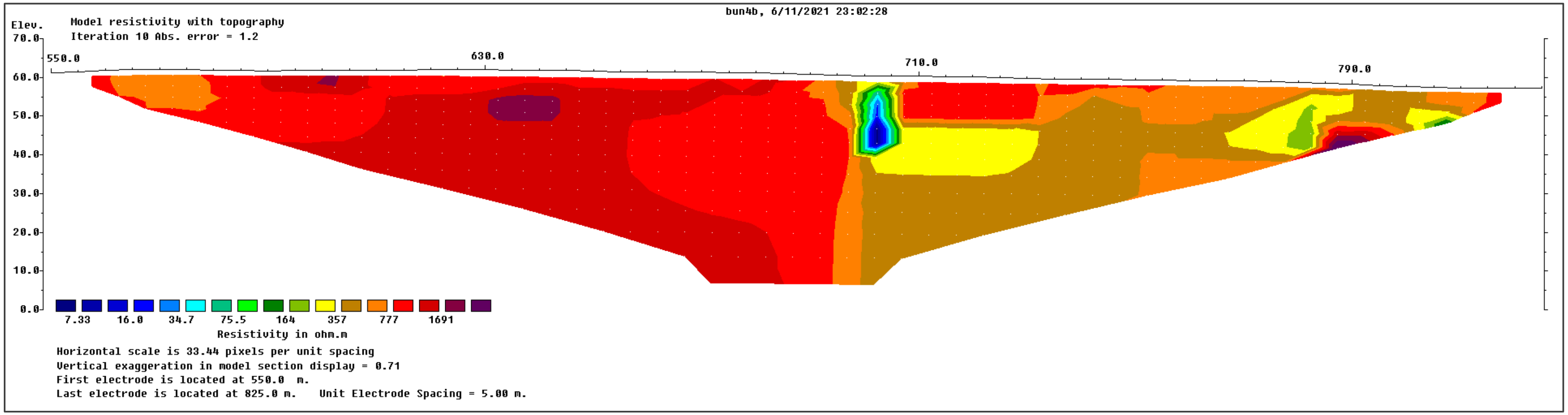

Figure A.12: Bun4b (Wenner).

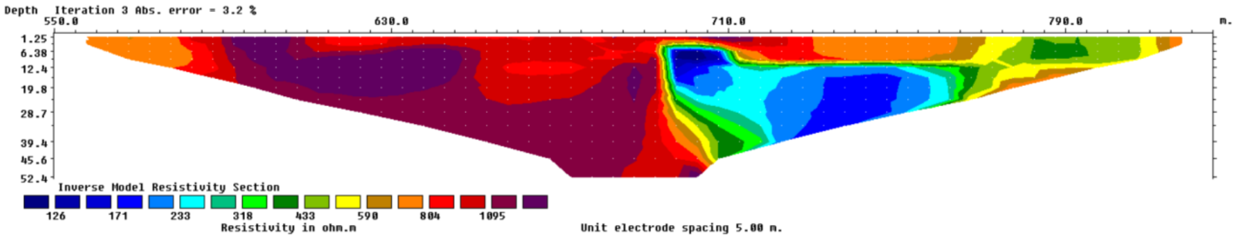

Figure A.13: Bun4b edited by manually changing res values in notepad. Note: no topography in model.

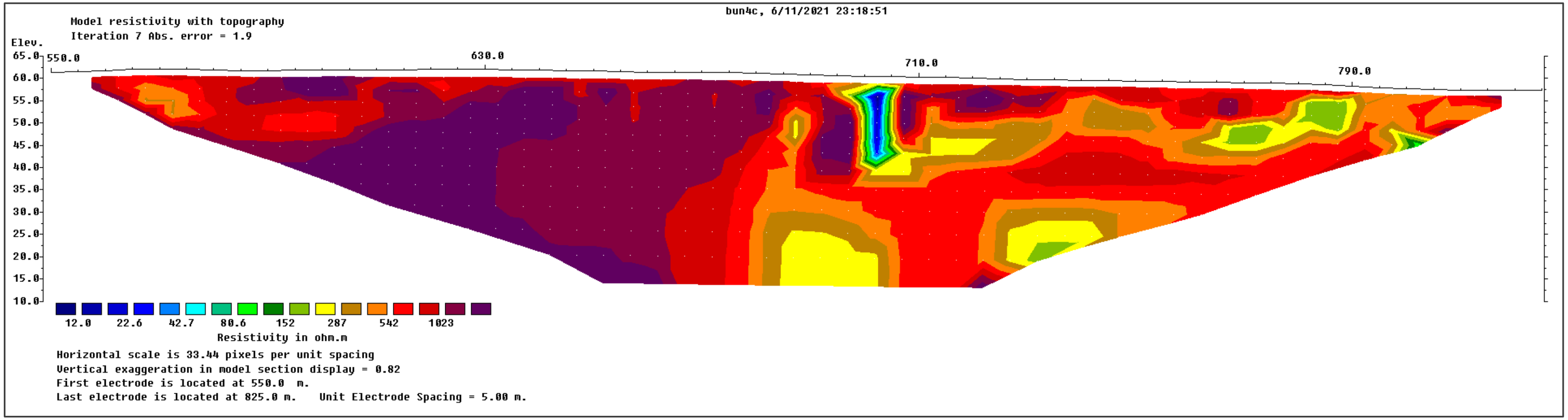

Figure A.14: Bun4c (Dipole-dipole).

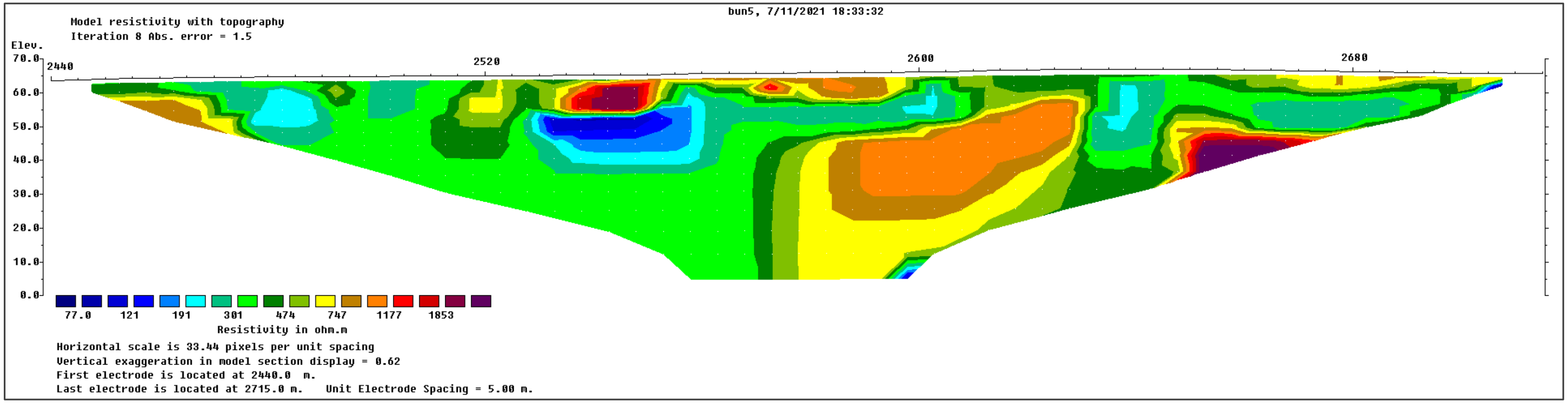

Figure A.15: Bun5 (Schlumberger).

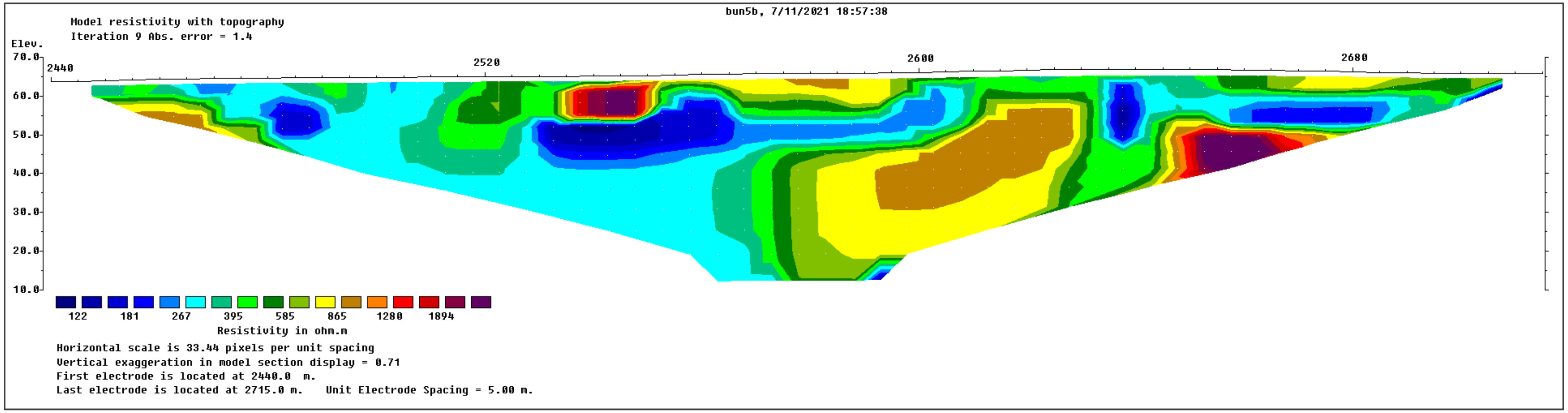

Figure A.16: Bun5b (Wenner).

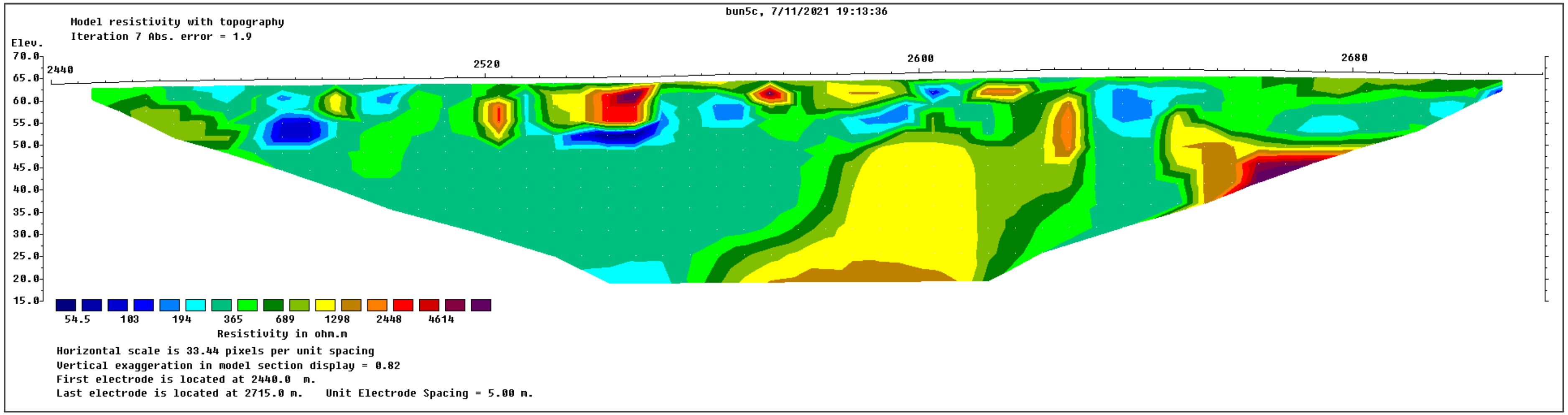

Figure A.17: Bun5c (Dipole-dipole).

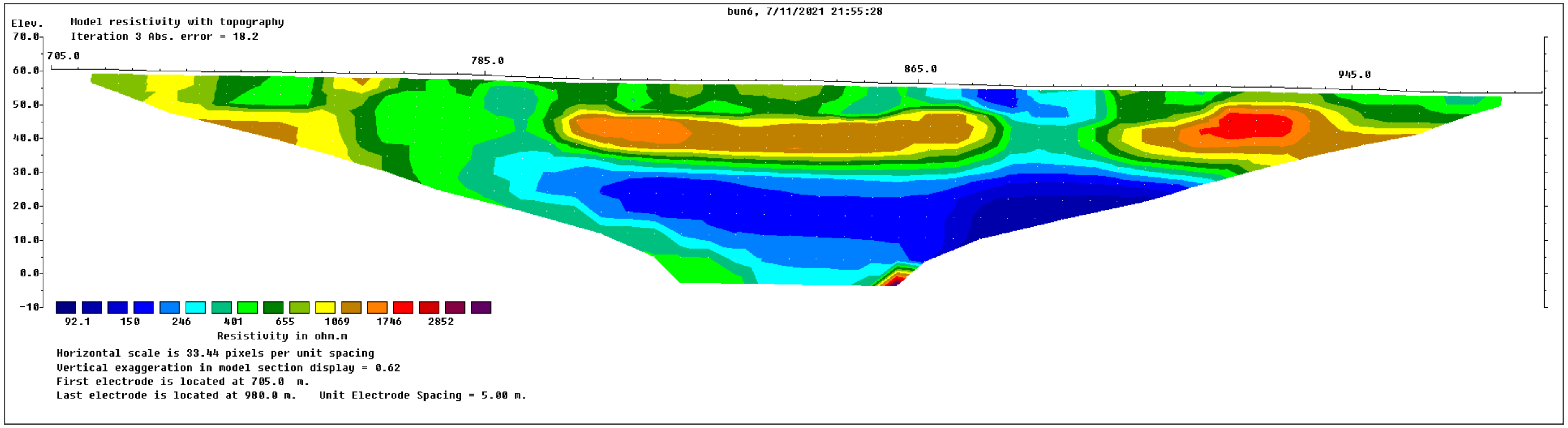

Figure A.18: Bun6 (Schlumberger).

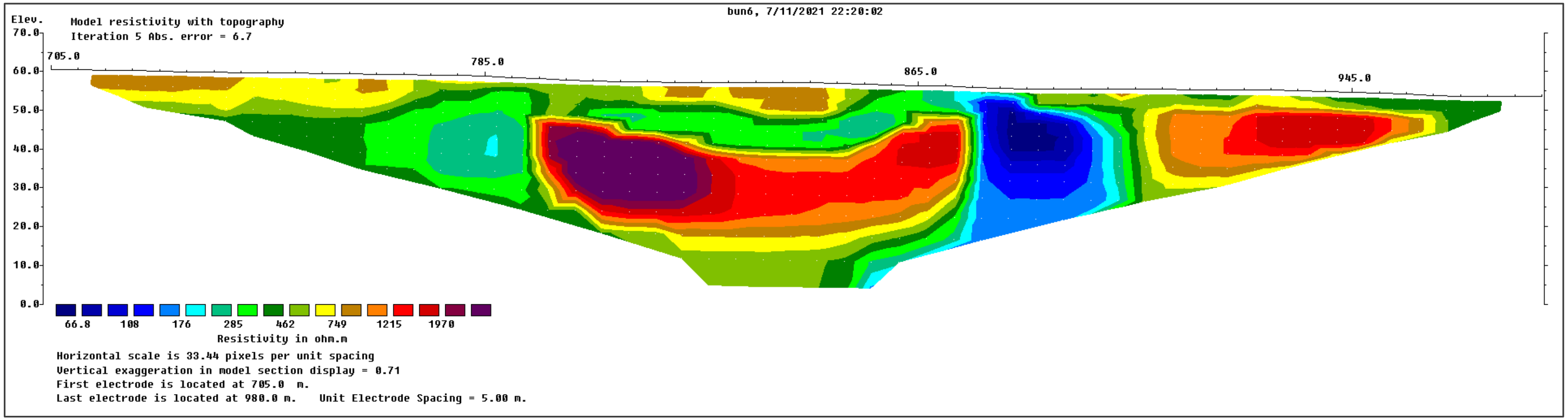

Figure A.19: Bun6b (Wenner).

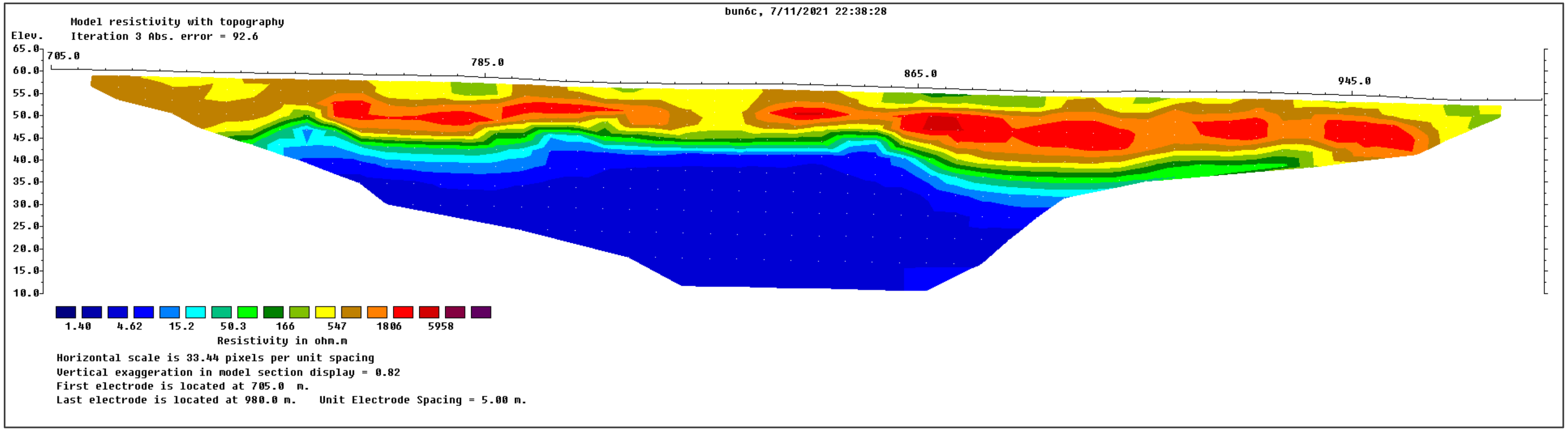

Figure A.20: Bun6c (Dipole-dipole).

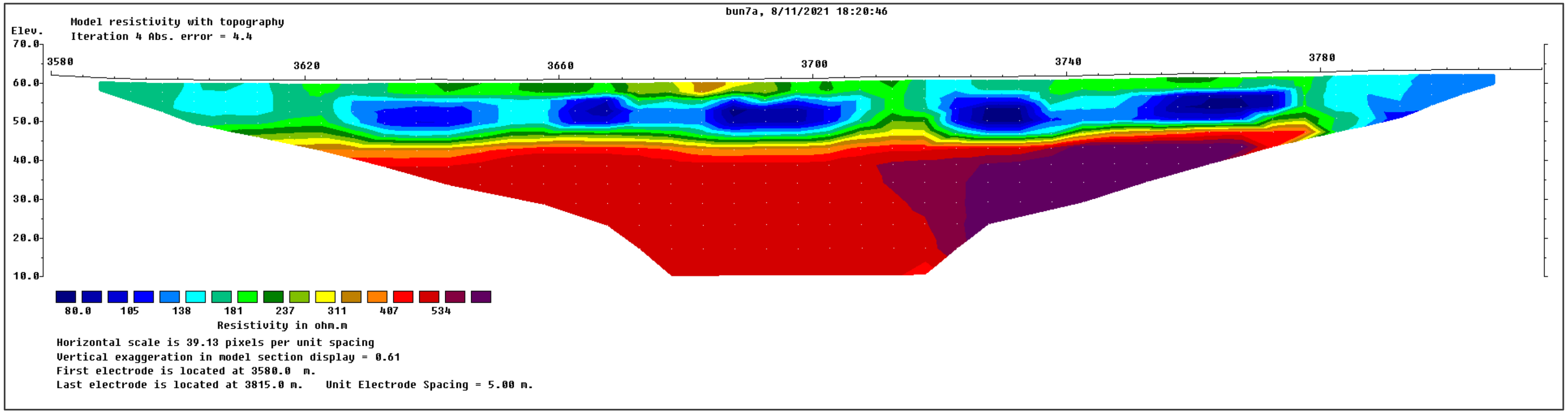

Figure A.21: Bun7 (Schlumberger).

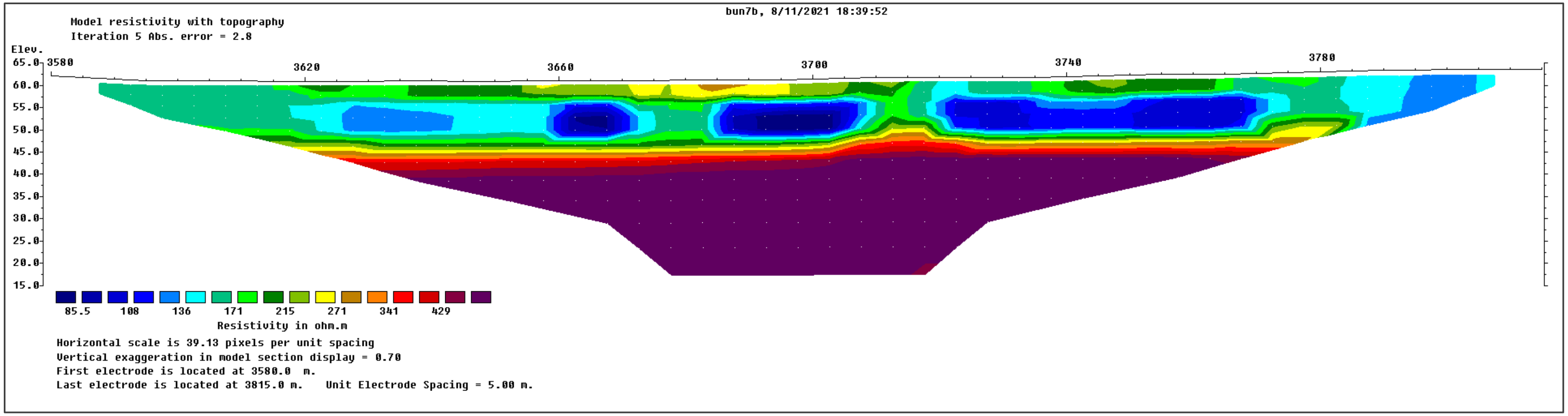

Figure A.22: Bun7b (Wenner).

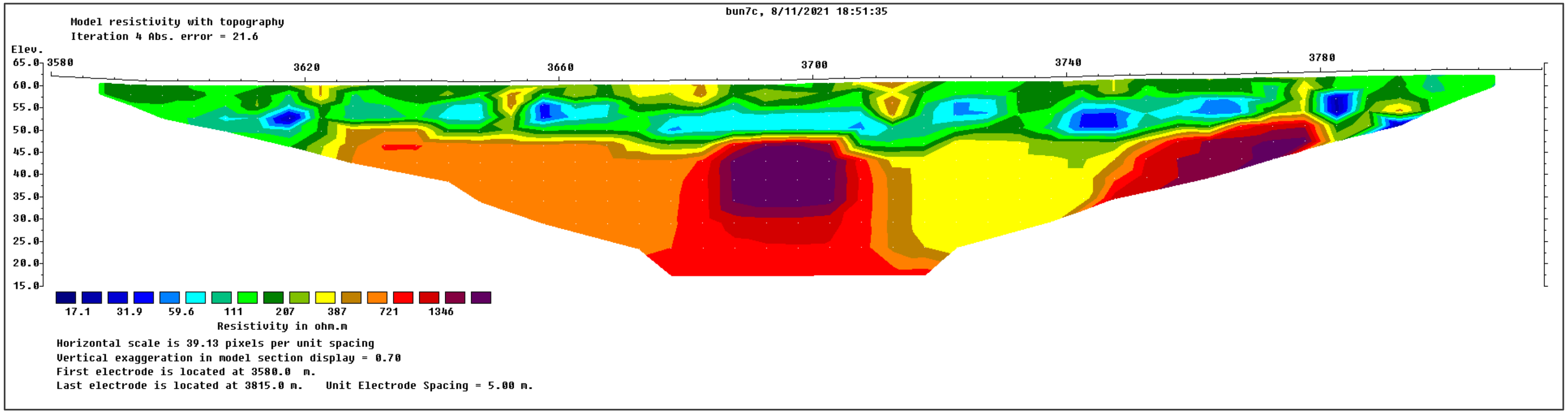

Figure A.23: Bun7c (Dipole-dipole).

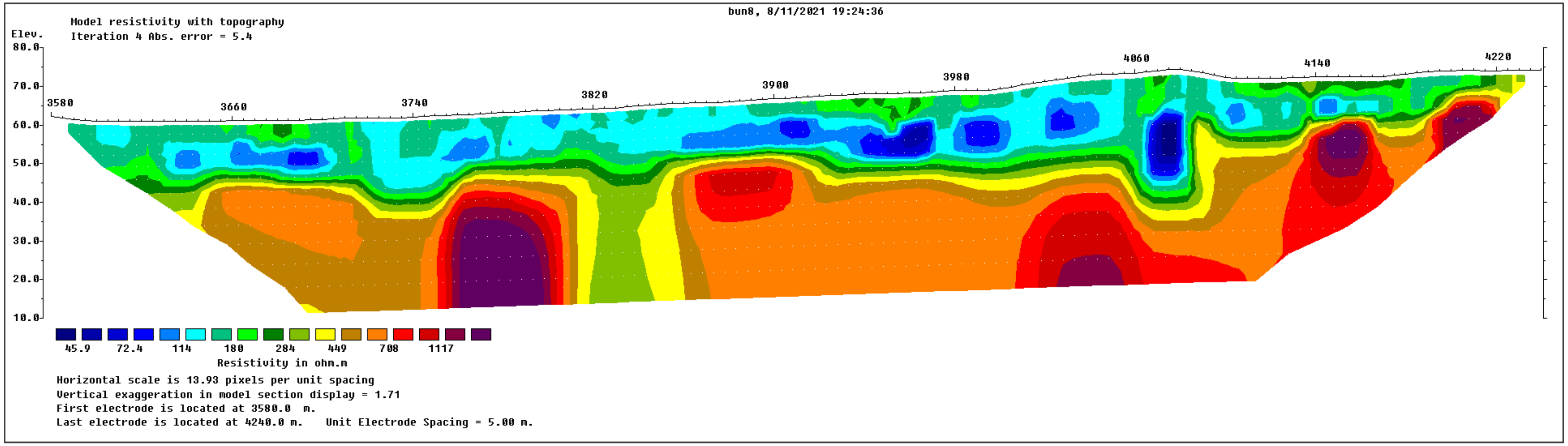

Figure A.24: Bun8 (Schlumberger).

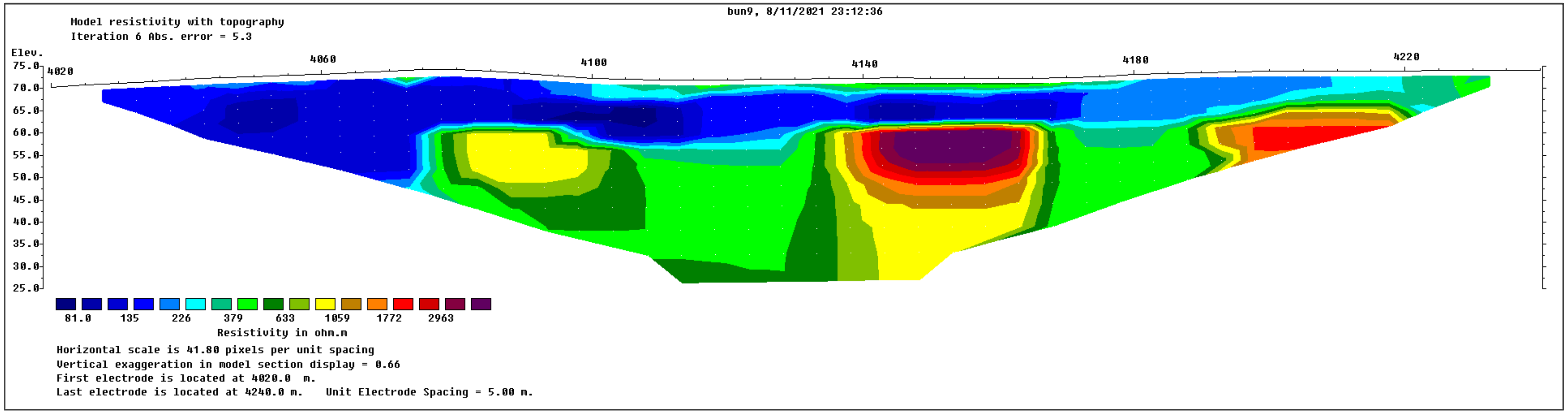

Figure A.25: Bun9 (Schlumberger).

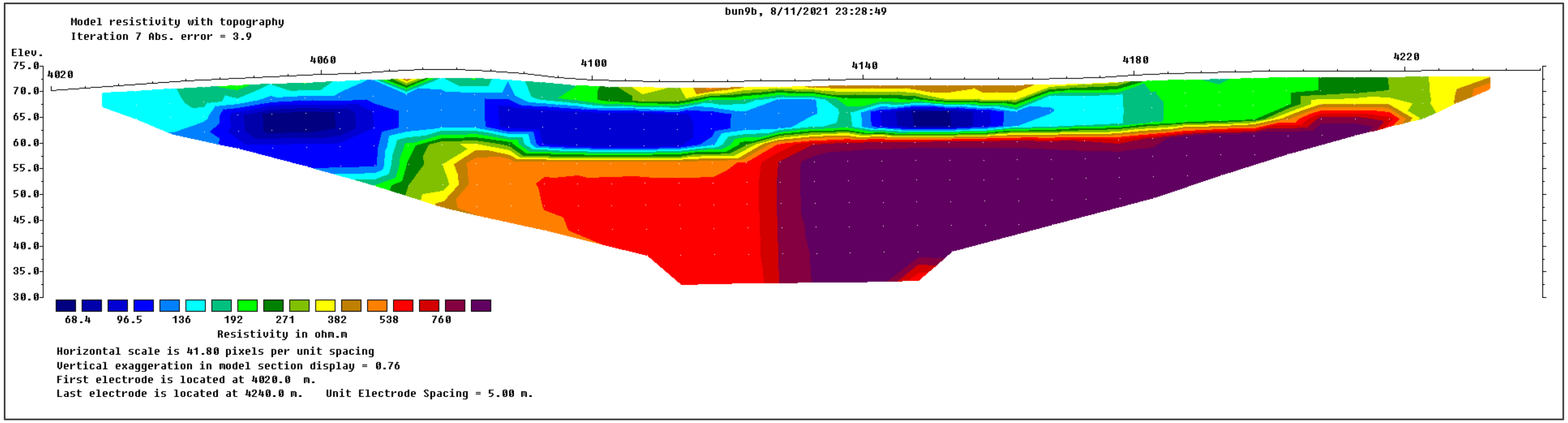

Figure A.26: Bun9b (Wenner).

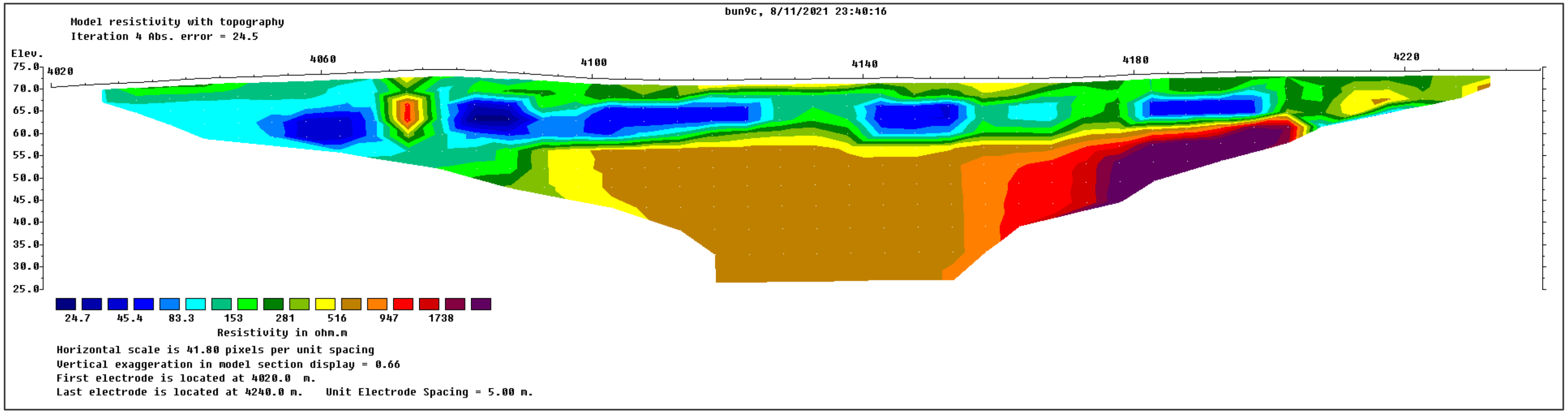

Figure A.27: Bun9c (Dipole-dipole).

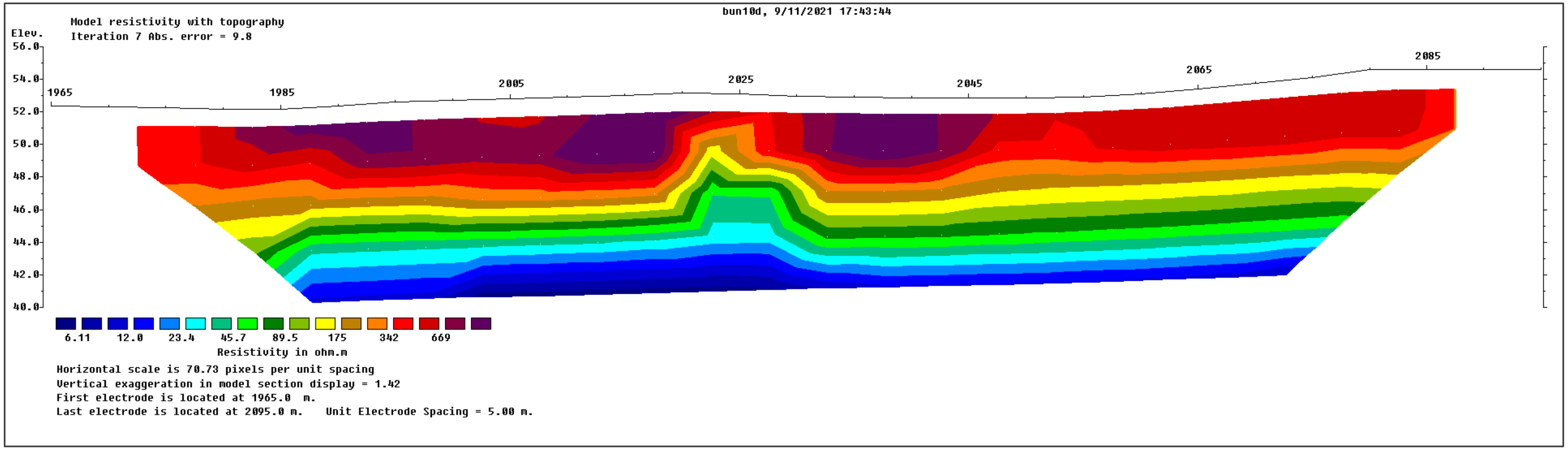

Figure A.28: Bun10d (Schlumberger).

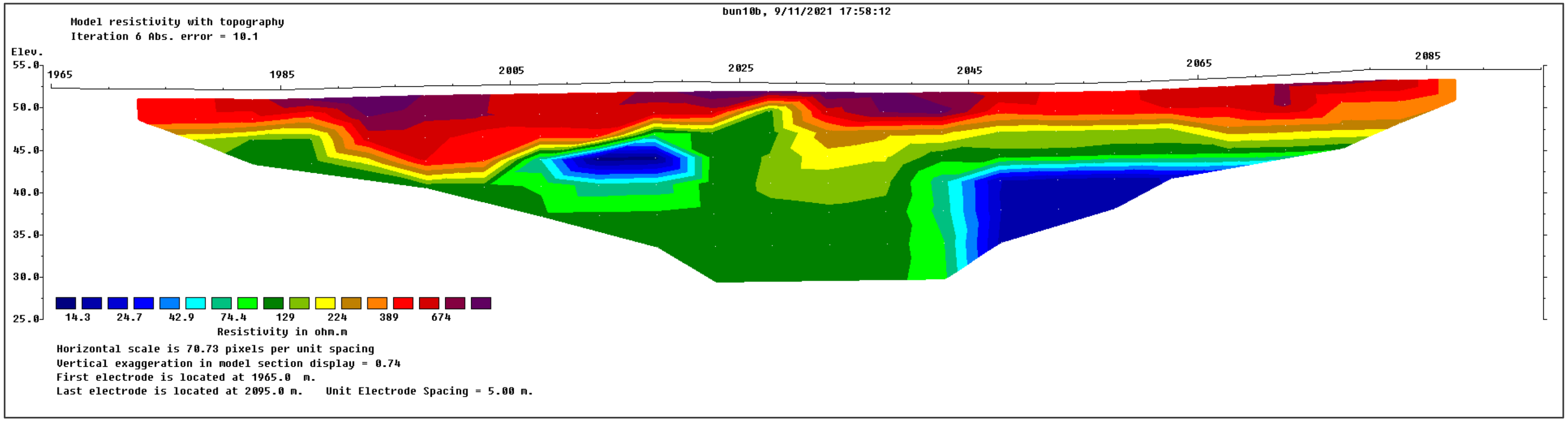

Figure A.29: Bun10b (Wenner).

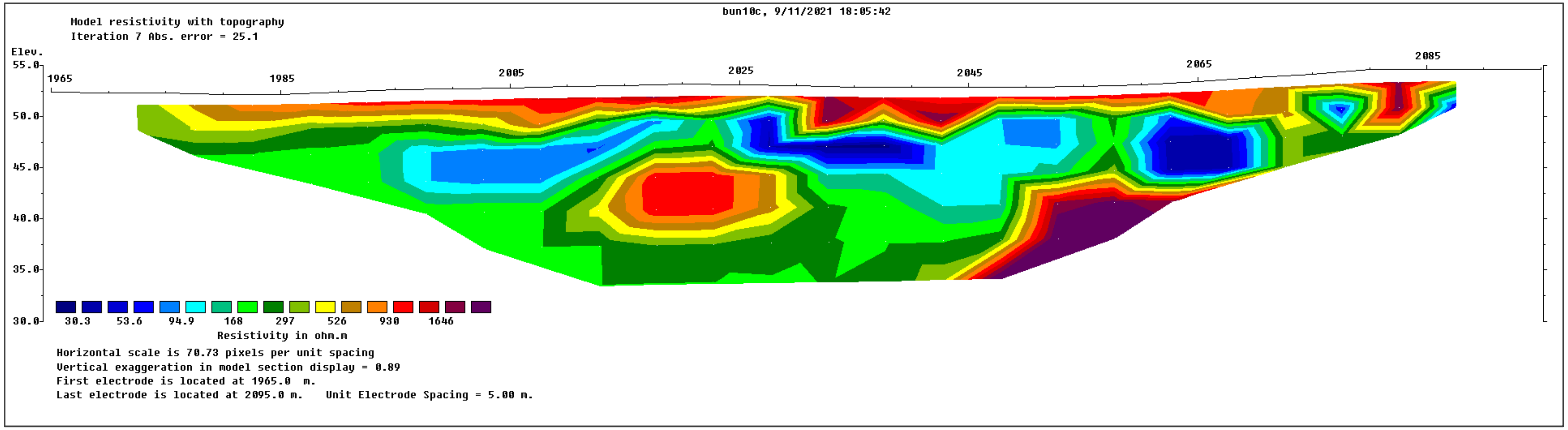

Figure A.30: Bun10c (Dipole-dipole).

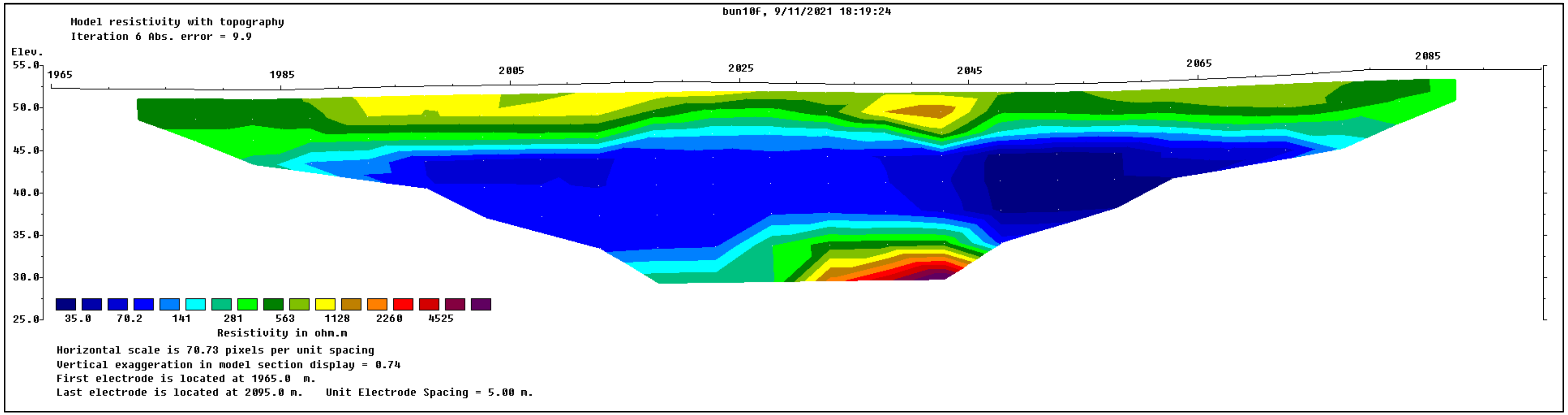

Figure A.31: Bun10f (Wenner; High Power).

Appendix B: Airborne EM Resistivity Models

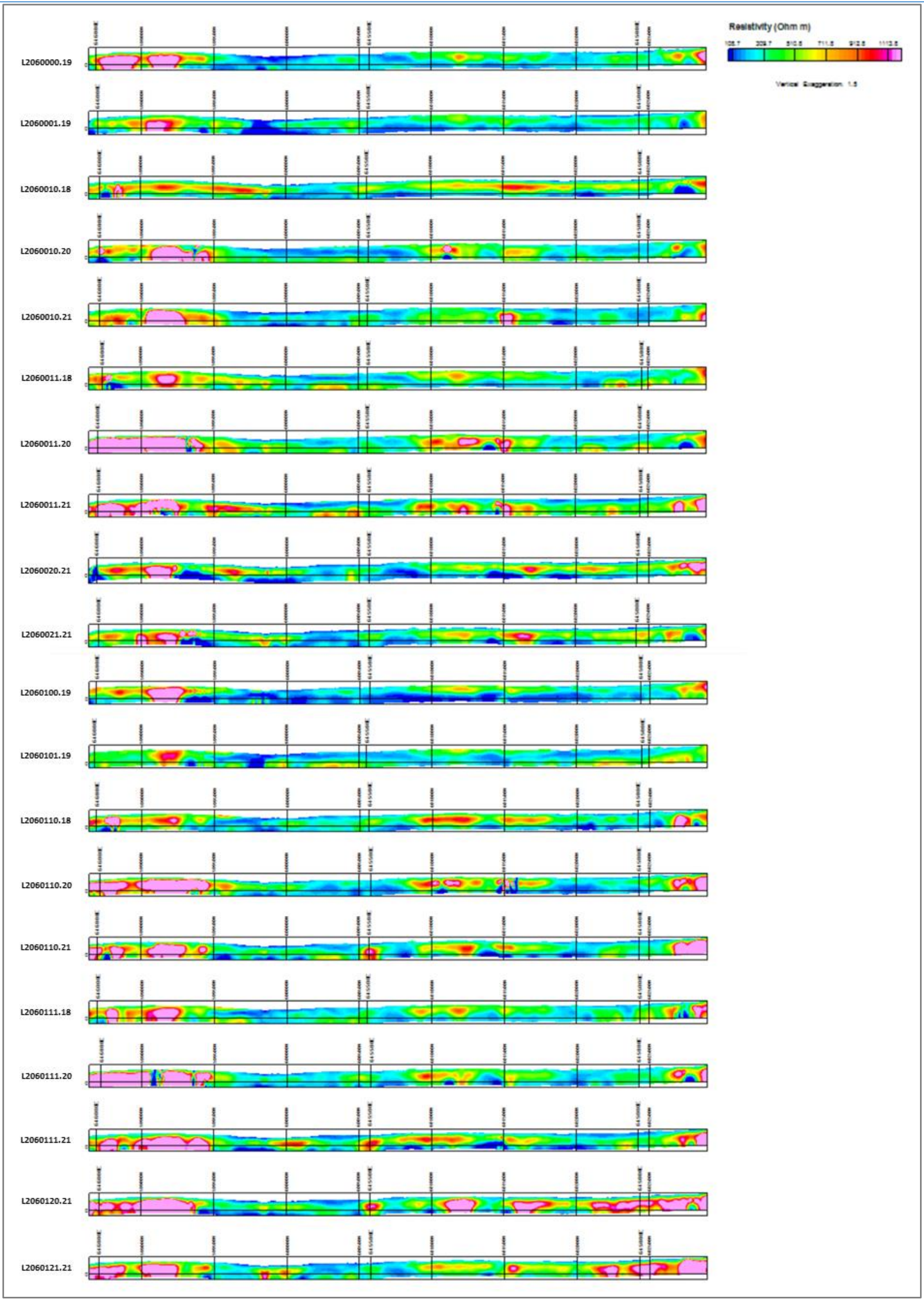

Figure B.1: Airborne EM inversion models for 20 flights along Waterford test line, all flown with nominal flight clearance of 60 m. Same linear colour scale and range of values used for each section. Sections are oriented South (left) to North (right). Vertical exaggeration = 1.5.

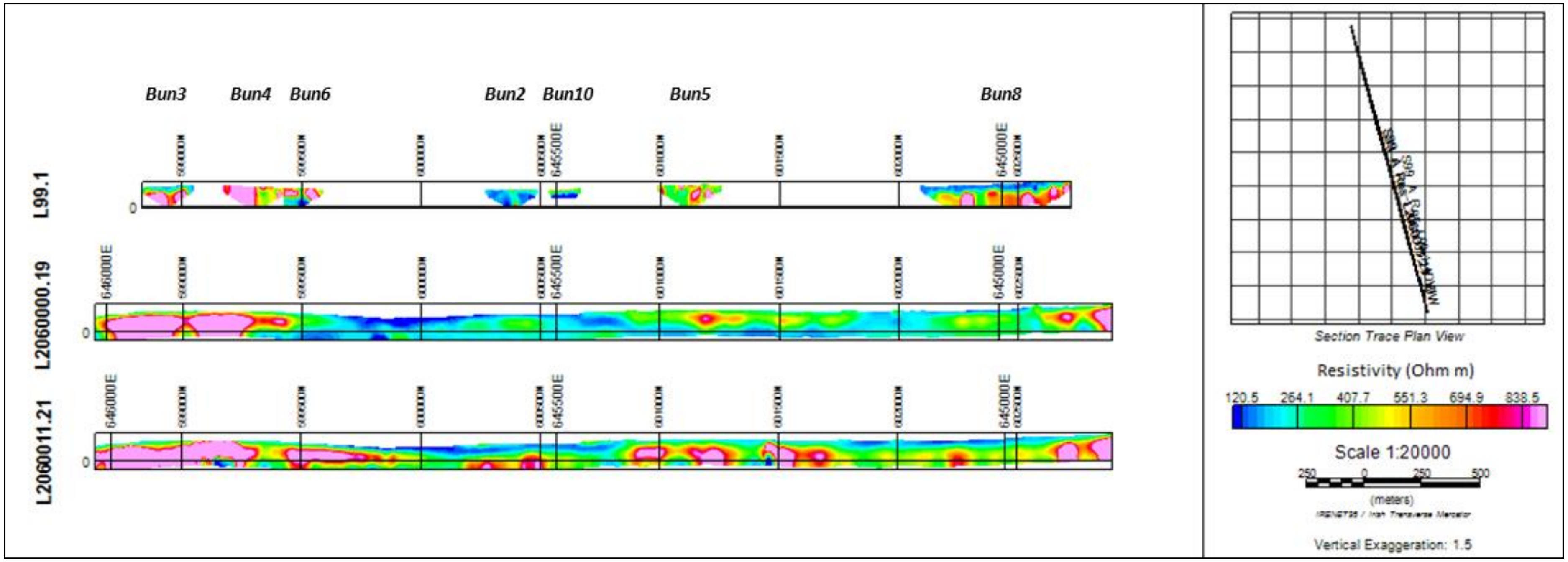

Figure B.2: ERT L99.1 (Schlumberger; all profiles joined) (top) and airborne EM L2060000.19 (middle) and L2060011.21 (bottom) inversion models. Linear colour scale and same range of values used. Sections are oriented South (left) to North (right). Vertical exaggeration = 1.5. Note the difference in maximum depths displayed for the EM and ERT profiles.

Appendix C: ERT and EM Model Sections

The following sections are oriented South (left) to North (right). All grids are coloured using the same linear colour scale, from minimum 100 Ωm (blue) to maximum 900 Ωm (pink).

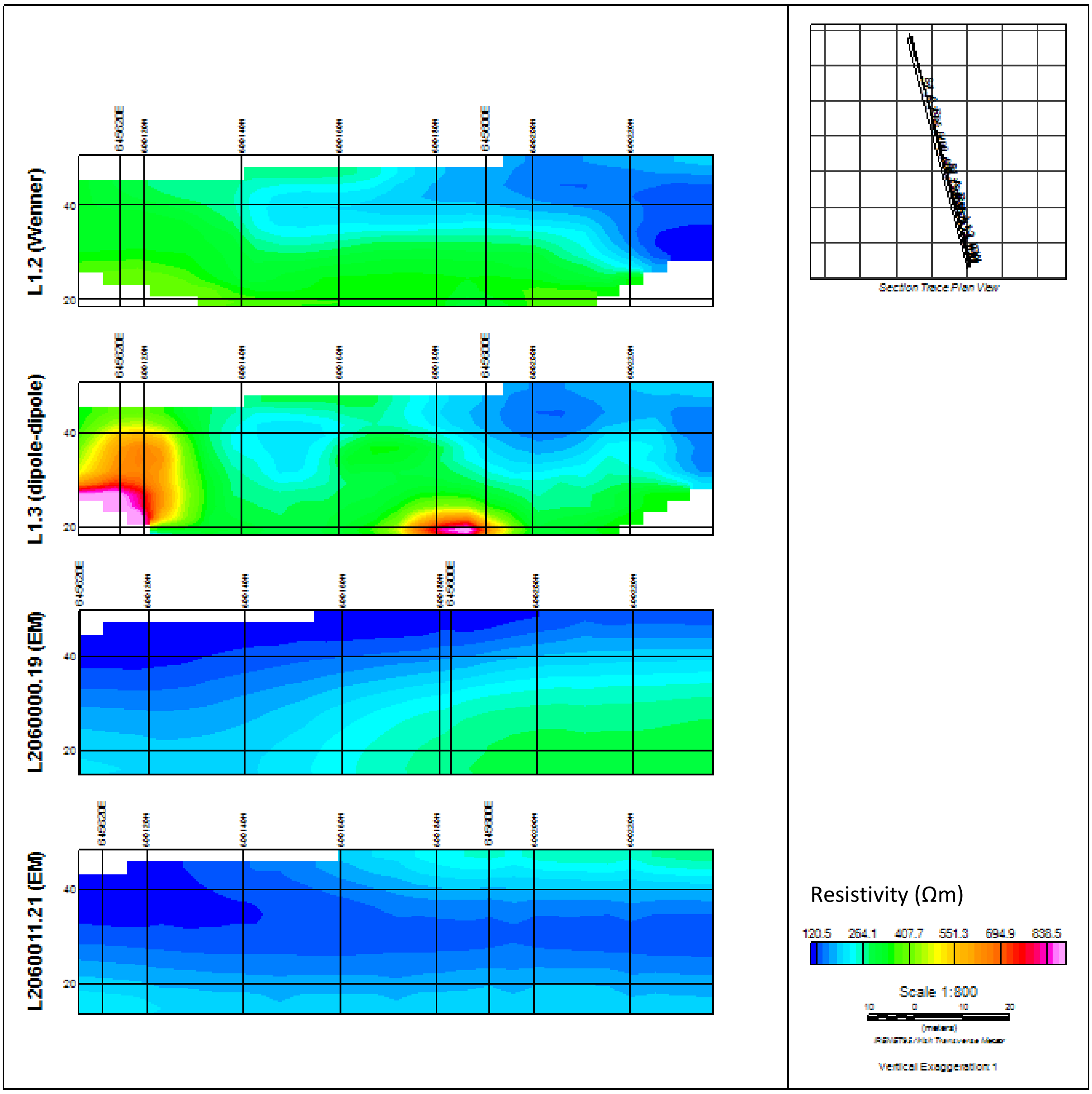

Figure C.1: Bun1 - Cropped ERT (Wenner and dipole-dipole) and selected EM (L2060000.19 and L2060011.21) inversion modelled sections.

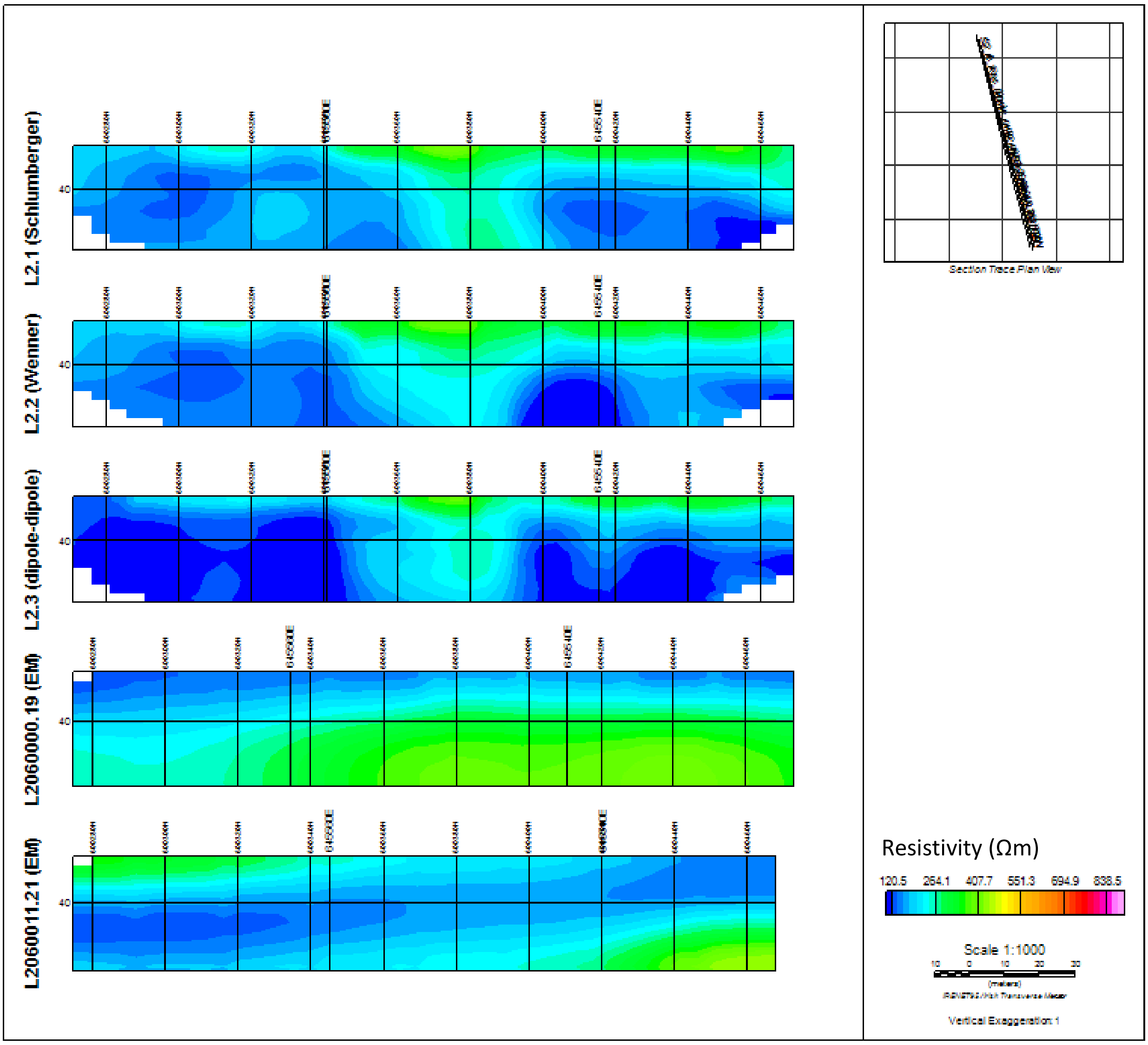

Figure C.2: Bun2 - Cropped ERT (Schlumberger, Wenner and dipole-dipole) and selected EM (L2060000.19 and L2060011.21) inversion modelled sections.

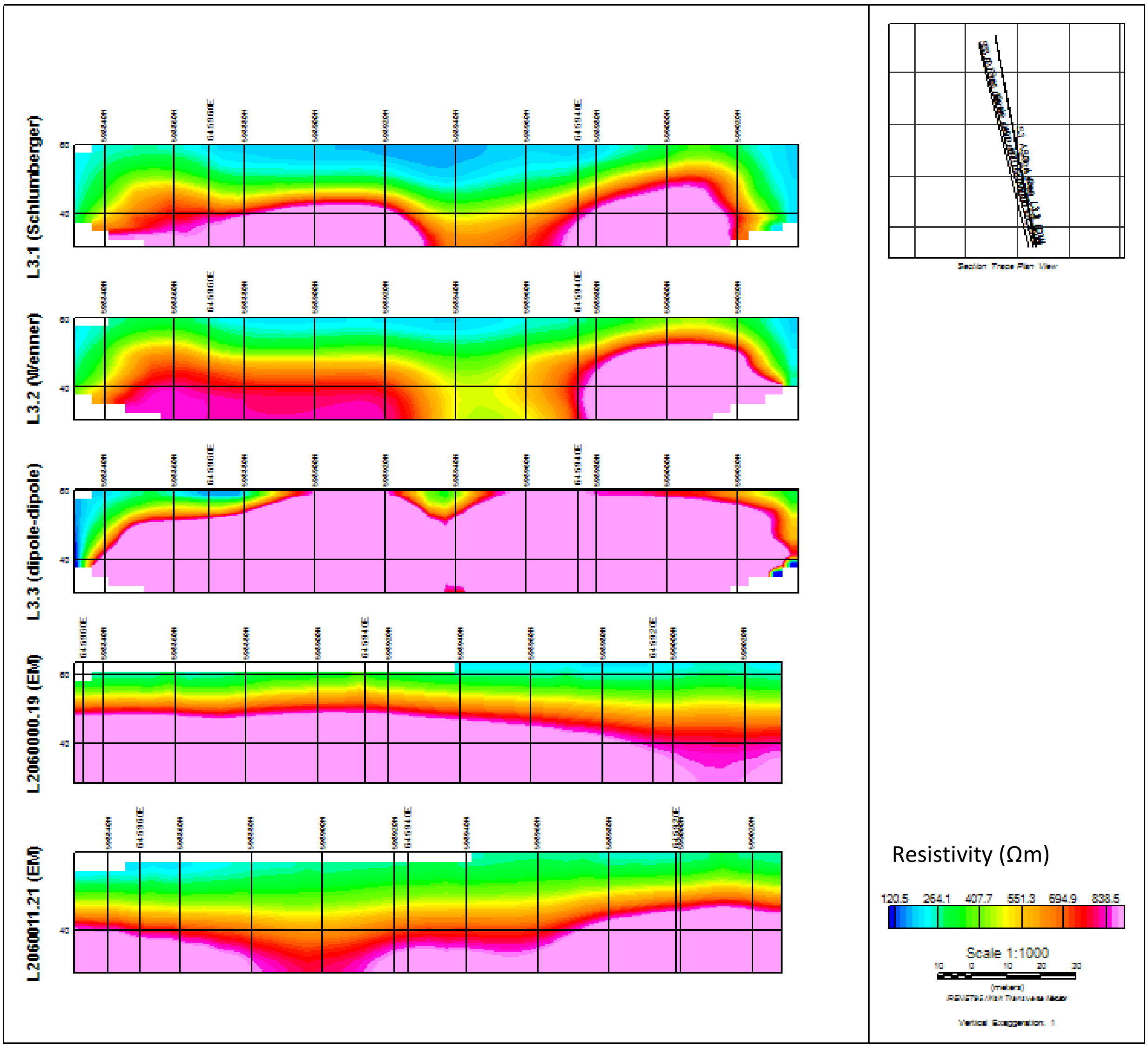

Figure C.3: Bun3 - Cropped ERT (Schlumberger, Wenner and dipole-dipole) and selected EM (L2060000.19 and L2060011.21) inversion modelled sections.

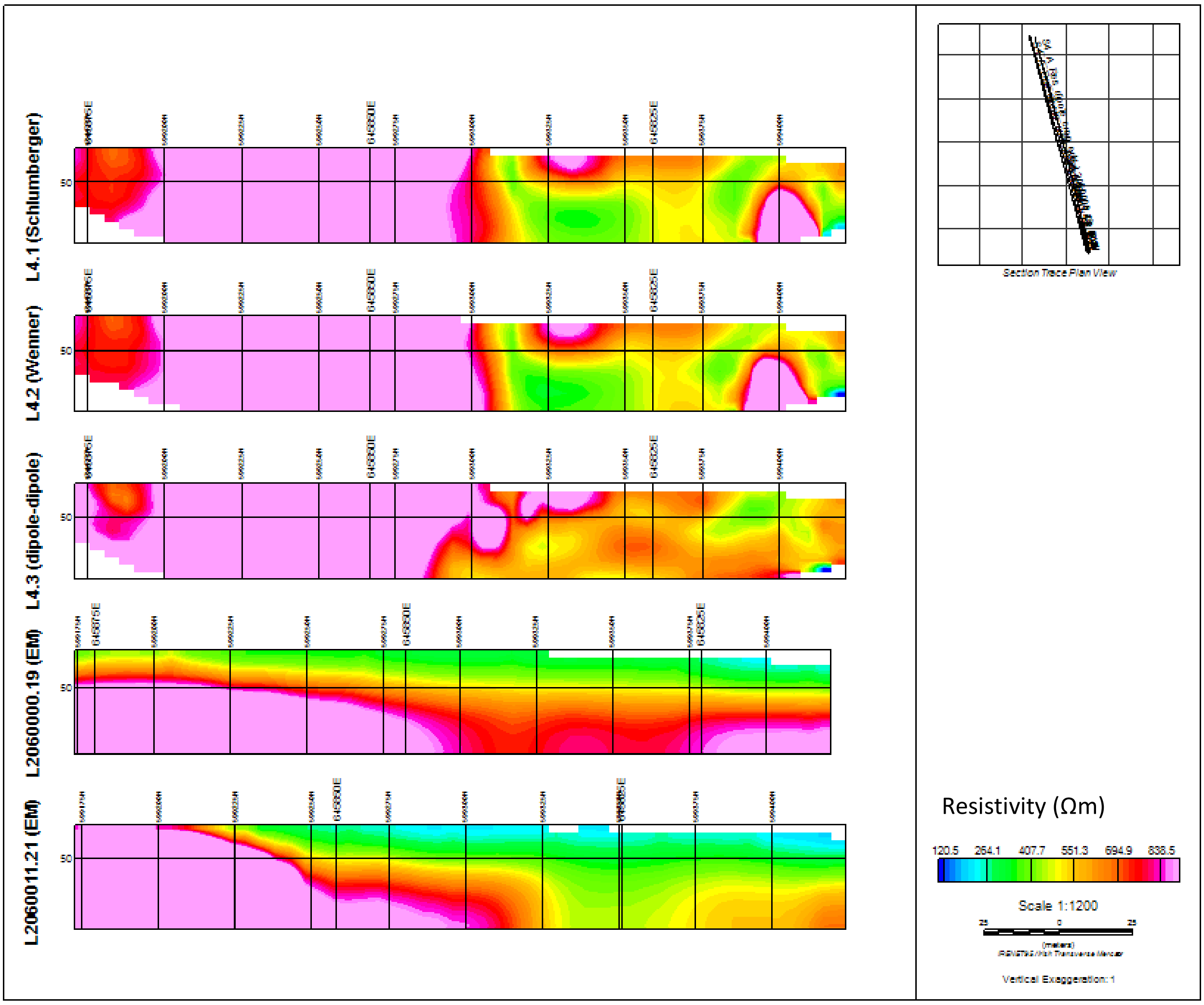

Figure C.4: Bun4 - Cropped ERT (Schlumberger, Wenner and dipole-dipole) and selected EM (L2060000.19 and L2060011.21) inversion modelled sections.

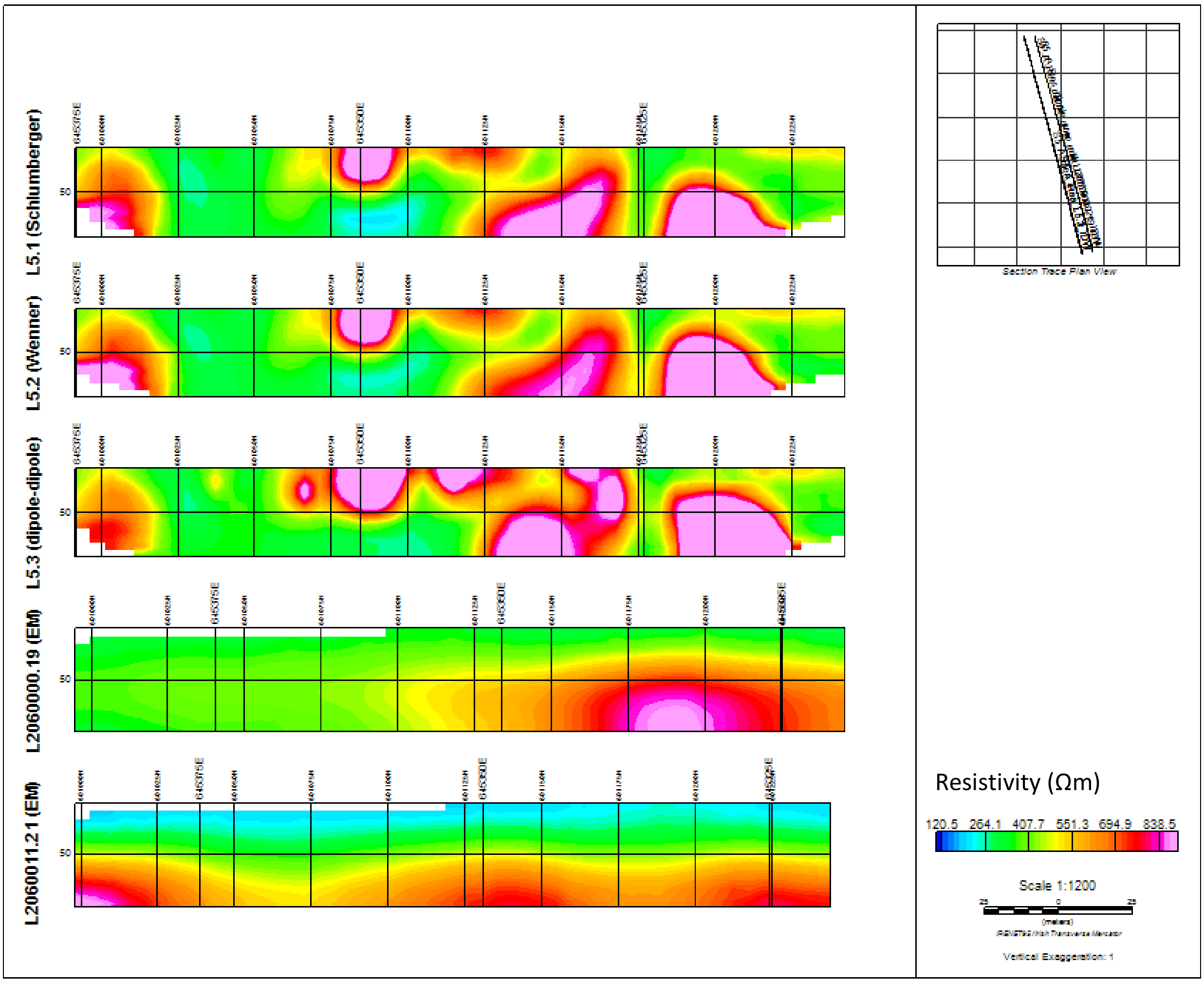

Figure C.5: Bun5 - Cropped ERT (Schlumberger, Wenner and dipole-dipole) and selected EM (L2060000.19 and L2060011.21) inversion modelled sections.

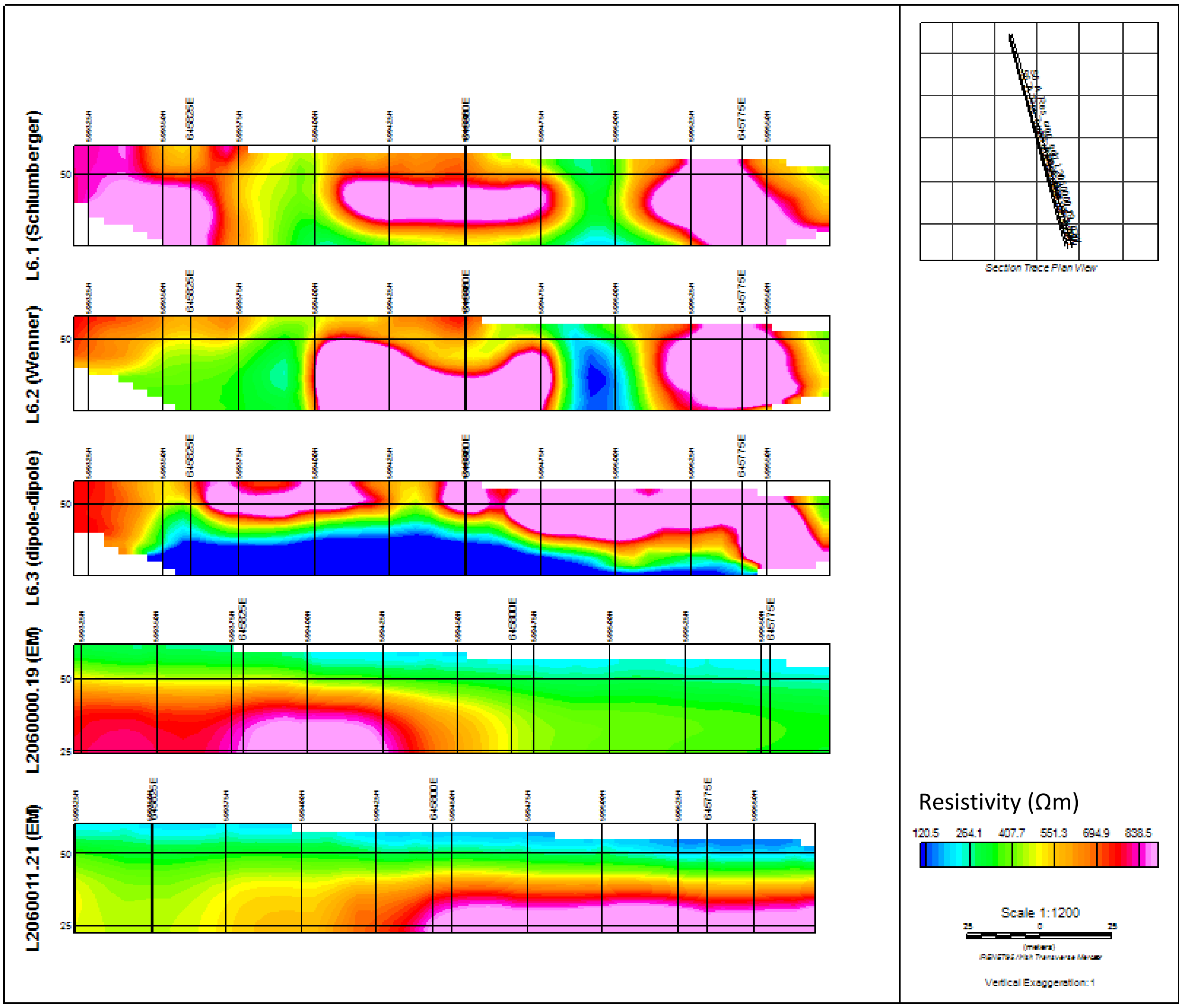

Figure C.6: Bun6 - Cropped ERT (Schlumberger, Wenner and dipole-dipole) and selected EM (L2060000.19 and L2060011.21) inversion modelled sections.

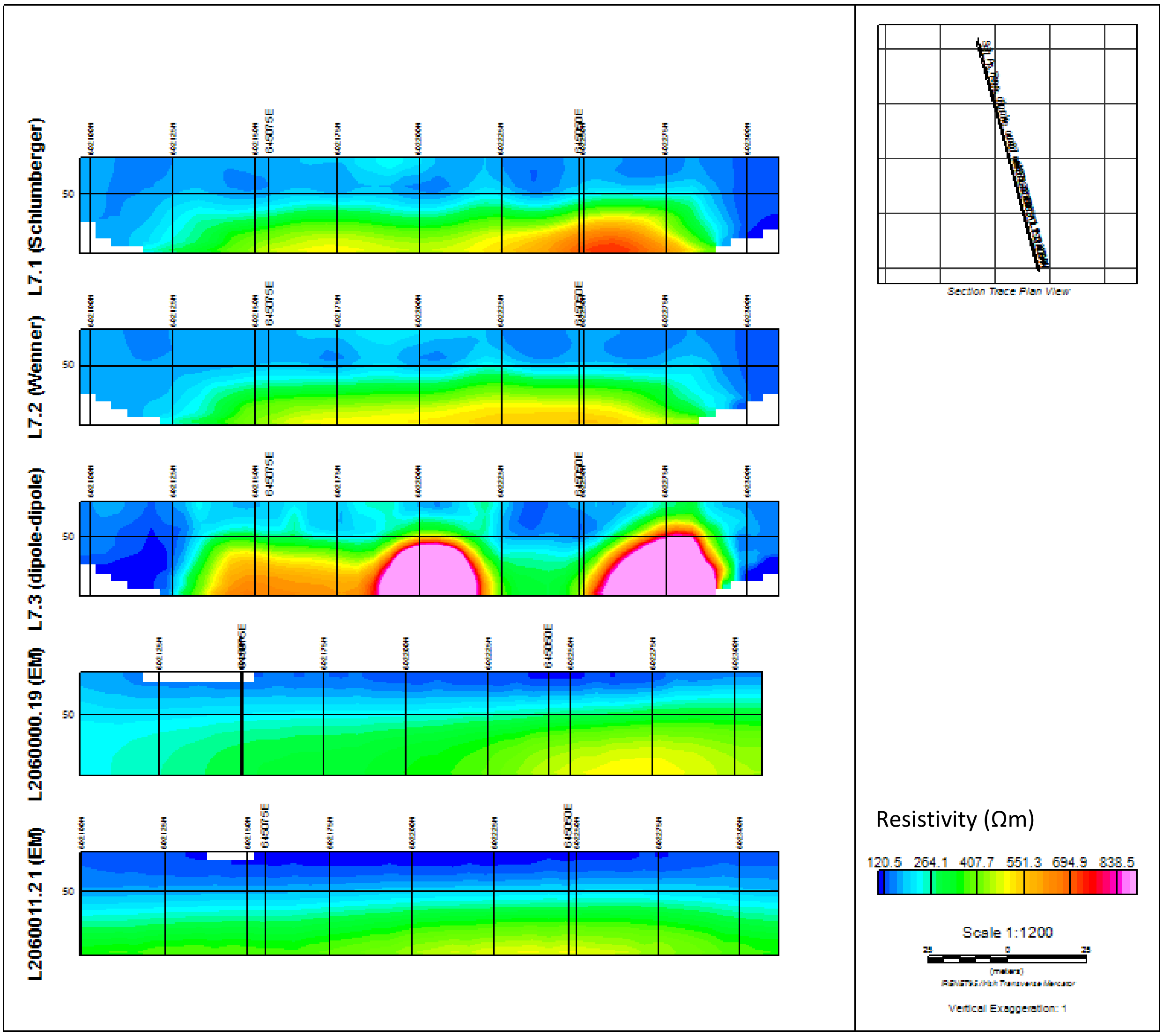

Figure C.7: Bun7 - Cropped ERT (Schlumberger, Wenner and dipole-dipole) and selected EM (L2060000.19 and L2060011.21) inversion modelled sections.

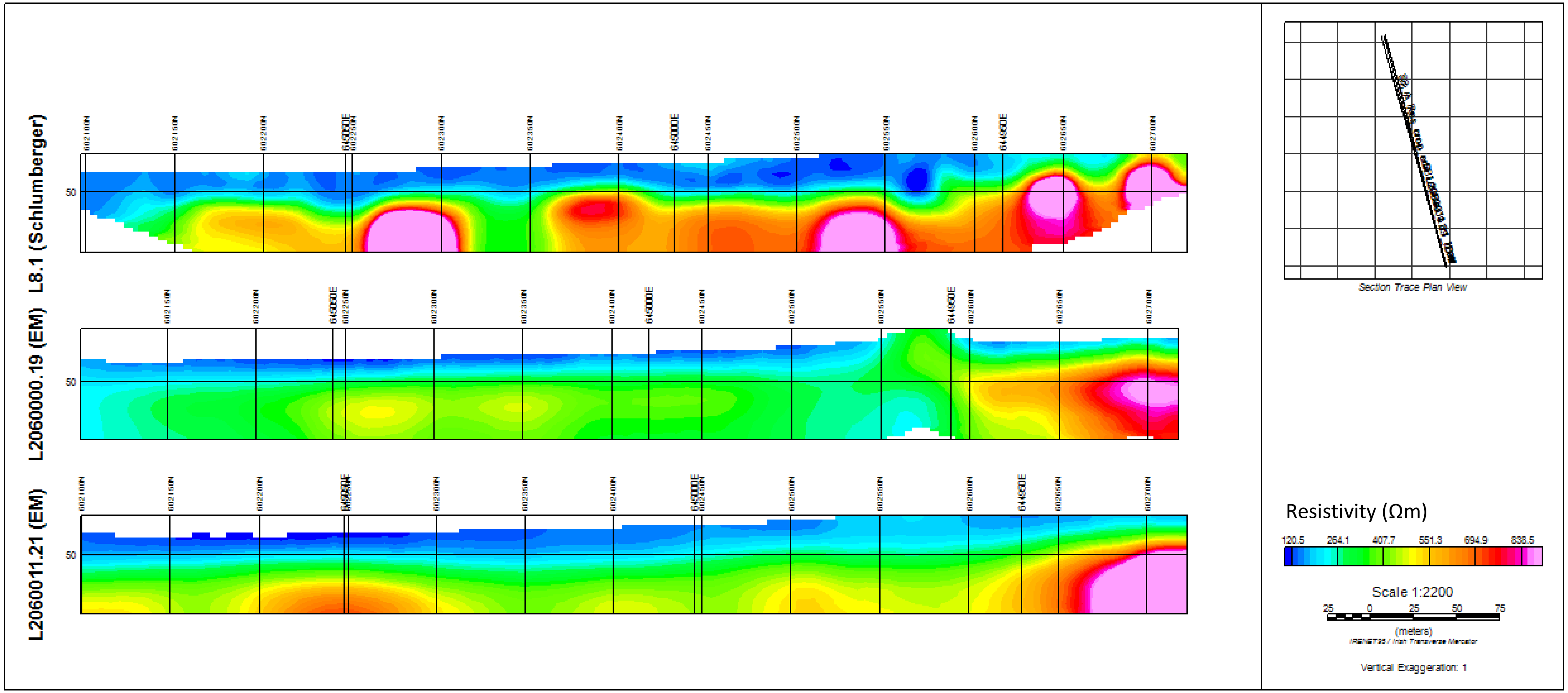

Figure C.8: Bun8 - Cropped ERT (Schlumberger) and selected EM (L2060000.19 and L2060011.21) inversion modelled sections.

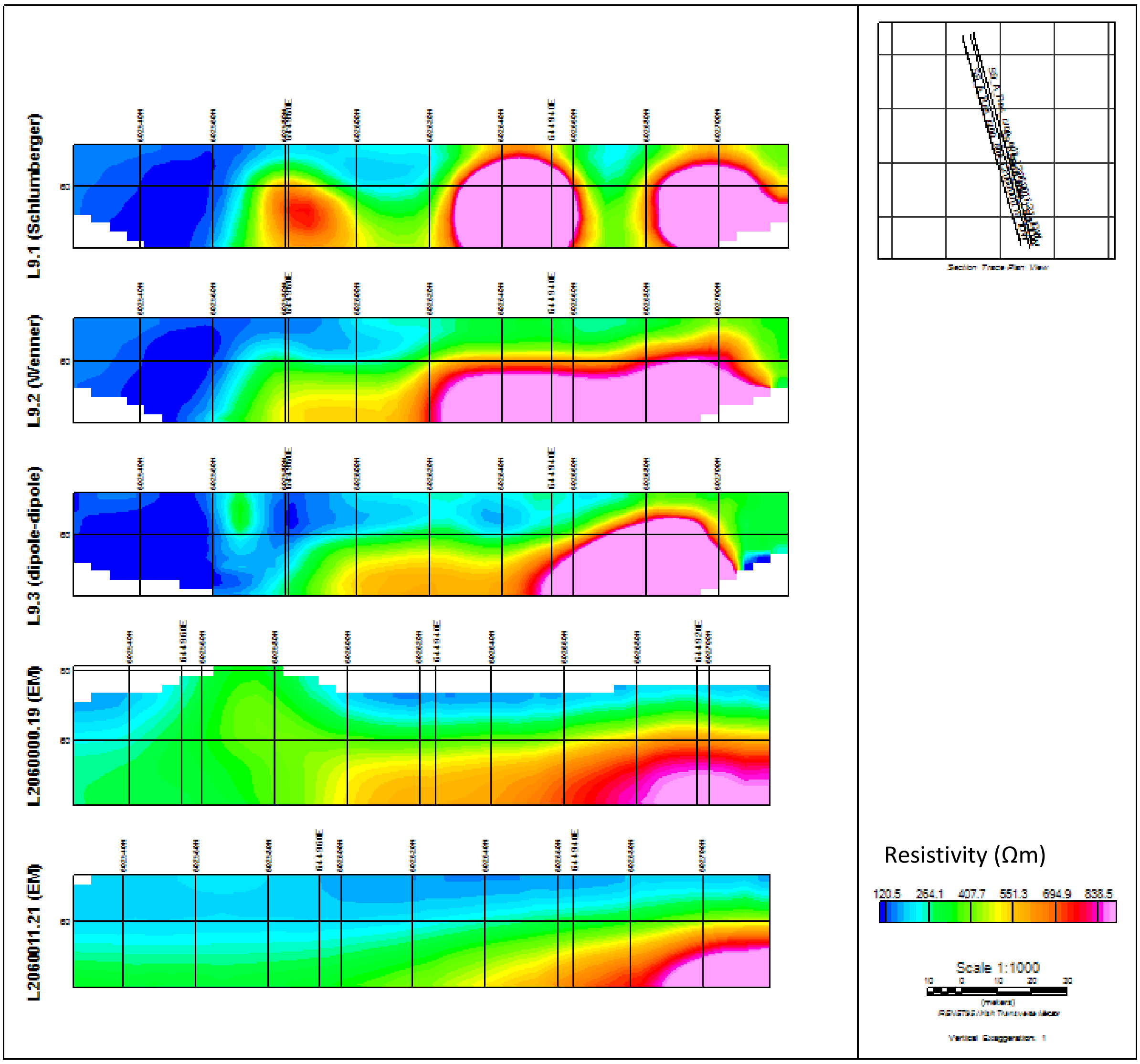

Figure C.9: Bun9 - Cropped ERT (Schlumberger, Wenner and dipole-dipole) and selected EM (L2060000.19 and L2060011.21) inversion modelled sections.

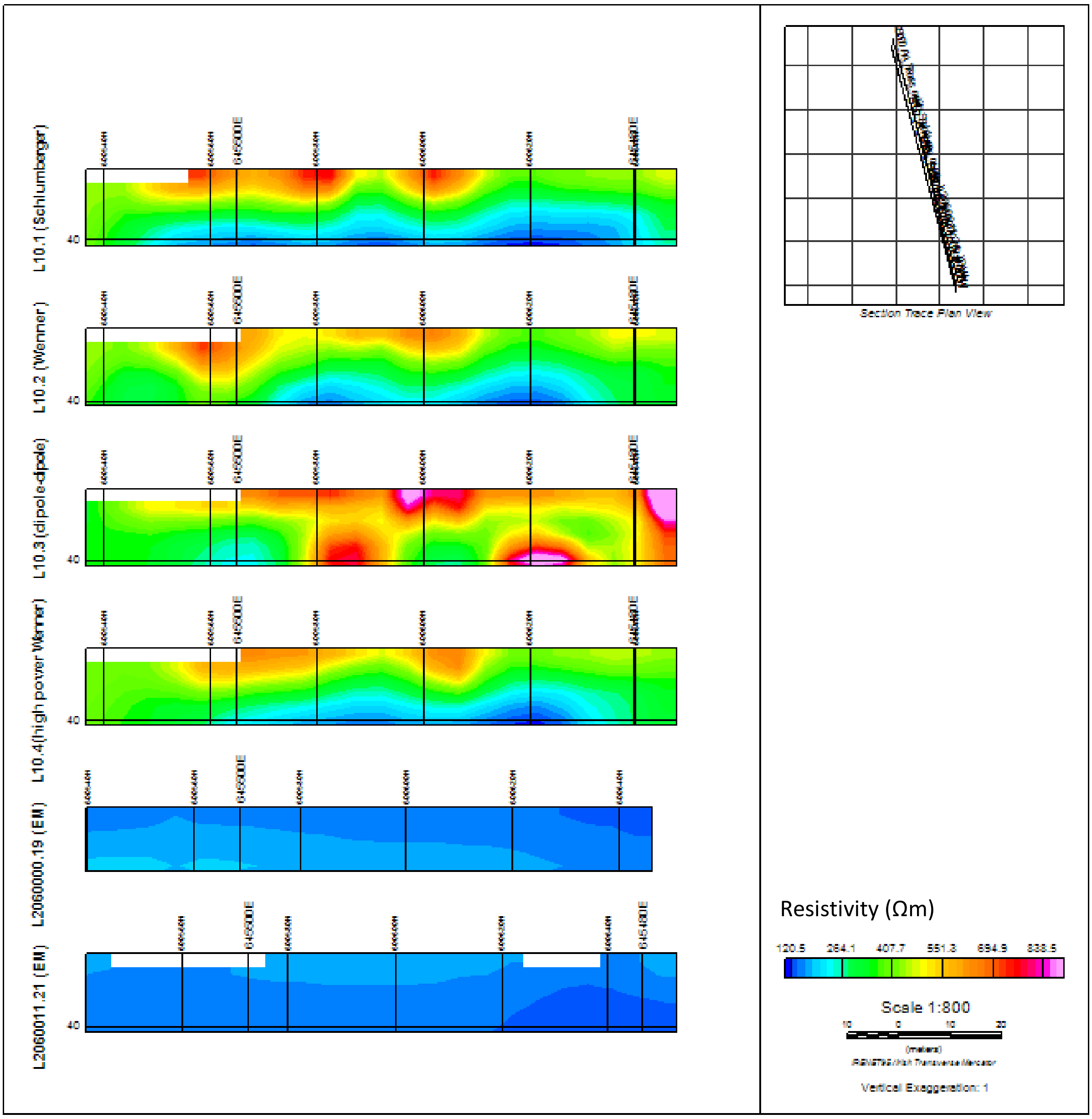

Figure C.10: Bun10 - Cropped ERT (Schlumberger, Wenner and dipole-dipole and high power Wenner) and selected EM (L2060000.19 and L2060011.21) inversion modelled sections.

Table C.1: Minimum, maximum, mean and standard deviation resistivity values (Ωm) for airborne EM models L2060000.19 and L2060011.21 and ERT models (Wenner, Schlumberger and dipole-dipole) along profiles Bun1 – Bun9 (shown in figures C.1 – C.9). Statistics are based on the original inversion model data. The airborne EM models are edited to exclude data < 1 Ωm and > 10,000 Ωm and clipped to match the depth extent of the ERT models (S = Schlumberger, W = Wenner, D = dipole-dipole). W and D depth extents are identical for all profiles.

		Bun1	**Bun2**	**Bun3**	**Bun4**	**Bun5**	**Bun6**	**Bun7**	**Bun8**	**Bun9**
EM: L2060000.19 clipped to S	*min*	-	87.5	91.0	148.9	207.8	148.9	66.6	66.6	92.6
	max	-	428.9	2670.9	1988.7	919.7	976.0	514.8	971.5	971.5
	mean	**-**	**269.8**	**1014.6**	**791.3**	**461.2**	**453.1**	**285.3**	**337.5**	**443.7**
	std dev	-	91.9	665.5	451.5	172.9	214.2	116.6	172.3	224.5
EM: L2060000.19 clipped to W/D	*min*	74.0	87.5	91.0	148.9	217.5	148.9	66.6	-	92.6
	max	302.7	428.9	2348.2	1887.7	919.7	976.0	514.8	-	971.5
	mean	**179.3**	**257.6**	**821.9**	**710.1**	**466.9**	**445.5**	**263.7**	**-**	**405.0**
	std dev	69.9	99.4	560.8	398.2	165.3	221.2	118.7	-	218.1
EM: L2060011.21 clipped to S	*min*	-	97.8	130.5	40.6	136.1	67.0	79.1	79.1	111.2
	max	-	822.5	2779.6	9421.6	1163.0	1228.4	745.7	1627.3	1627.3
	mean	**-**	**272.7**	**853.0**	**1196.9**	**509.0**	**568.2**	**317.1**	**340.8**	**432.3**
	std dev	-	156.4	578.4	1789.3	253.8	321.6	176.1	235.9	333.0
EM: L2060011.21 clipped to W/D	*min*	99.4	97.8	130.5	40.6	136.1	67.0	79.1	-	111.2
	max	419.4	552.9	1998.4	9421.6	994.5	1138.0	556.7	-	1365.0
	mean	**168.8**	**205.2**	**630.6**	**1215.7**	**414.8**	**479.3**	**241.7**	**-**	**327.4**
	std dev	68.1	86.0	408.3	2005.4	201.9	282.1	127.2	-	227.8
ERT: Schlumberger	*min*	-	32.5	123.8	8.0	68.7	91.7	74.8	40.9	71.2
	max	-	1544.6	1711.2	5442.4	3270.5	2248.9	749.9	1874.4	5634.8
	mean	**-**	**217.9**	**549.5**	**851.0**	**533.4**	**619.6**	**290.3**	**393.0**	**592.8**
	std dev	-	141.0	470.6	441.7	431.1	411.1	188.3	334.9	897.3
ERT: Wenner	*min*	73.5	58.2	124.3	6.0	110.7	59.2	80.7	-	62.8
	max	464.1	676.9	1712.5	4468.0	3090.6	3605.4	572.7	-	1167.5
	mean	**244.7**	**216.7**	**506.6**	**851.9**	**548.2**	**774.6**	**247.6**	**-**	**435.6**
	std dev	109.9	126.4	389.4	431.9	471.1	736.4	153.3	-	363.6
ERT: Dipole-Dipole	*min*	48.2	-33.8	1.3	10.2	46.5	3.1	17.7	-	21.2
	max	1728.9	815.7	10161.0	2263.4	10193.0	3762.8	2933.7	-	3715.6
	mean	**281.2**	**179.7**	**2832.5**	**904.6**	**651.1**	**657.6**	**407.7**	**-**	**445.0**
	std dev	237.1	147.2	3433.0	465.7	945.4	812.7	529.3	-	663.3

Table C.2: Minimum, maximum, mean and standard deviation resistivity values (Ωm) for airborne EM models L2060000.19 and L2060011.21 and ERT models (Wenner, Schlumberger and dipole-dipole) along profile Bun10 (shown in figure C.10). Statistics are based on the original inversion model data. The airborne EM models are edited to exclude data < 1 Ωm and > 10,000 Ωm and clipped to match the depth extent of the ERT models (S = Schlumberger, W = Wenner, D = dipole-dipole).

Bun10	*min*	*max*	***mean***	*std dev*
EM: L2060000.19 - clipped to S	110.1	212.6	**153.4**	28.6
EM: L2060000.19 - clipped to W	110.1	254.1	**179.1**	40.2
EM: L2060000.19 - clipped to D	110.06	251.12	**173.91**	38.8
EM: L2060011.21 - clipped to S	120.4	212.8	**154.2**	18.9
EM: L2060011.21 - clipped to W	120.4	264.7	**170.4**	33.9
EM: L2060011.21 - clipped to D	120.38	226.96	**162.26**	24.26
ERT: Schlumberger	5.2	1548.4	**370.3**	384
ERT: Wenner	12.4	1342	**332.6**	294.1
ERT: Dipole-Dipole	26.3	3359.1	**574.8**	694.4
ERT: Wenner (high power)	29.5	10781	**454.1**	1020.7